von Karman Institute for Fluid Dynamics
Aeronautics/Aerospace Department

Development of a unified model for flow-material interaction applied to porous ablators

Master thesis presented by **Joffrey Coheur**
Von Karman Institute for Fluid Dynamics, academic year 2015-2016.

Supervisor:

Prof. T. Magin (VKI)

Advisors:

A. Turchi (VKI)

P. Schrooyen (Cenaero)

Abstract

During the atmospheric reentry phase of a spacecraft, a huge amount of heat is exchanged between the surrounding air and the thermal protection system of the vehicle. The ablation of carbon-resin composite materials used for the heat shield is a very complex multi-physic problem. The degradation phenomenon occurs mainly in two steps. First, the resin is progressively pyrolysed, producing pyrolysis gases and a char matrix. Then, the char is ablated simultaneously by chemical reactions, sublimation and spallation.

The objective of this work is to simulate the degradation of thermal protection materials inside the VKI Plasmatron facility by considering the contribution of the pyrolysis in the ablation process. The study is performed in two steps.

First, the ablation of a non-charring porous material (carbon preform) inside the Plasmatron facility is reproduced by means of the Argo code, developed at Cenaero in collaboration with the VKI. The free-stream boundary conditions corresponding to the Plasmatron test is first thoroughly reviewed for their implementation in the code. Then, the flow through and around the carbon preform sample is simulated.

The second step consists is the development and the implementation of a new module of the DGAblation branch of Argo to model the pyrolysis of the material. The code is validated on several test cases, and the simulation of a full pyrolysis and ablation problem of a carbon-phenolic material inside the Plasmatron is finally performed.

It is the first time that strongly coupled simulations of the degradation of a thermal protection material corresponding to those largely tested in the Plasmatron is performed.

Results of the simulations show good agreement with the surface temperature measurements. Numerically, a mesh fine enough, at least lower than the length of ablation, is required at the interface to catch the recession of the surface. The flow inside the material can also be extracted from the simulations. The Stokes flow percolates through the porous medium toward the shoulders of the material and at the same time products of reactions are released in the boundary layer. A simple Plasmatron simulation on carbon-phenol provides similar observations on the flow field.

These results demonstrate the ability of the unified approach together with a discontinuous galerkin discretization to solve ablation problems on simple carbon preform as well as on ablative composite materials. With the new model accounting for the pyrolysis, the code features a unique capability to simulate the flow around and within ablative composite material.

Acknowledgments

Even the shortest projects are never carried out alone and we always need someone experienced to teach less experienced ones. This section is devoted to all the people that helped my during this Research Master project.

First of all I would like to thanks my supervisor and advisors. To all of them, thank you for giving me the opportunity to work on this very interesting topic and for the support you provided me during this one year project.

I would like to thanks Prof. Thierry Magin for all the time he spent helping me on all the aspect of the project, the time spent for helping me on the presentations and the final report and all the interesting thoughts and advices given.

I would like to thanks Alessandro Turchi for being always available for me and for all the interesting discussions we had. Thank you deeply for the constant follow-up you provided me and for your patience.

During this project, I also had the opportunity to work in collaboration with Cenaero. Therefore, I would like to thank Koen Hillewaert and the whole Argo team for hosting me during several weeks.

In particular, I would like to deeply thanks Pierre Schrooyen for all the time he spent (that I could not even count) helping me to understand this huge program which is Argo, the help he provided from the very beginning and to the development of the numerical implementation of this project, and until the end of the project. Without your help, I would not have been able to carry out this project.

I would like to thanks all the people who helped me during the achievement of this thesis. I would like to thanks Bernd Helber for helping me on the understanding of the experimental part and for his inspiring work. I would like to thanks Vincent Leroy for helping me to think and for his advices when I got stuck. I would like also to thanks all the reviewer of this final report.

I could not end up this acknowledgements section without mentioning all the Research Master students. We have spent one year together, we had a lot of fun but also days harder than others, sometimes spending the entire night working. But always you have been there for support and good times. So this is why I would like to thanks all you, for sharing together this experience and making it great!

Of course, all my gratitude is again addressed to my family, for all the support and always being there for me.

Contents

List of Figures

List of Tables

List of Symbols

Acronyms

AUSM	Advection Upstream Splitting Method
CBCF	Carbon-Bonded Carbon Fiber
CFD	Computational Fluid Dynamics
CGFEM	Classical Galerkin Finite Element Method
DGM	Discontinuous Galerkin Method
DOF	Degrees of Freedom
ESA	European Space Agency
FEM	Finite Element Method
FVM	Finite Volume Method
GMRES	Generalized Minimal Residual Method
HSC	High-Speed Camera
ICP	Inductively-Coupled Plasma
ILU	Incomplete LU
LHTS	Local Heat Transfer Simulation
LTE	Local Thermodynamic Equilibrium
MHD	Magnetohydrodynamics
MPI	Message Passing Interface
NASA	National Aeronautics and Space Administration
NR	Newton-Raphson
NS	Navier-Stokes
NSI	Non-Symmetric Interior Penalty
OpenMP	Open Multi-Processing
PICA	Phenolic Impregnated Carbon Ablator
QoI	Quantity of Interest
REV	Representative Elementary Volume
SIP	Symmetric Interior Penalty
SLAU	Simple Low Dissipation AUSM
TACOT	Theoretical Ablative Composite for Open Testing
TPM	Thermal Protection Material
TPS	Thermal Protection System
VANS	Volume-Averaged Naver-Stokes
VKI	von Karman Institute

Roman Symbols

A_0	Arrhenius rate coefficient	s^{-1}
c_p	Specific heat at constant pressure	$\mathrm{J\ kg^{-1}\ K^{-1}}$

c_v	Specific heat at constant volume	J kg^{-1} K^{-1}
Ea	Arrhenius activation energy	J mol^{-1}
f_i	Velocity distribution function of species i	m^6 s^{-3}
f_i^M	Maxwellian velocity distribution function of species i	m^6 s^{-3}
k_f	Forward reactivity	m s^{-1}
k_B	Boltzmann's constant	J K^{-1}
$\dot{m}$	Injected gas mass flow rate	g s^{-1}
M	Mach number	
M_{cl}^r	Relative Mach number for the centerline jet value	-
M_{cl}^r	Relative Mach number for the ambient stream	-
$\mathscr{M}$	Mixture molar weight	kg
N_A	Avogadro's number	-
n^S	Number of species in the mixture	-
p_{tc}	Static pressure in the test chamber	Pa
P_{el}	Power provided by the high-frequency generator	W
P_{fl}	Power transmitted to the plasma flow	W
$\mathcal{R}$	Universal gas constant	J K^{-1}
S	Sutherland's temperature	K
T	LTE temperature	K
$\boldsymbol{u}$	Hydrodynamic velocity	m s^1
u	Radial velocity component	m s^{-1}
v	Azimuthal velocity component	m s^{-1}
w	Streamwise velocity component	m s^{-1}

Greek Symbols

γ	Specific heat ratio	-
λ	Thermal conductivity	W m^{-1} K^{-1}
μ	Dynamic viscosity	kg m^{-1} s^{-1}
ρ	Density	kg m^{-3}

Mathematical Notation and Operators

$\langle\cdot\rangle$	Superficial average operator
$\langle\cdot\rangle_\gamma$	Intrinsic average on a general phase γ

Subscripts

$_f$	Fibers
$_g$	Gas
$_m$	Matrix
$_s$	Solid
$_\infty$	Freestream value

Chapter 1

Introduction

Motivation

Atmospheric entry problem

One of the most challenging step in space missions is the design of the heat shield for spacecraft, used to protect them from the severe aerothermal environment achieved during the atmospheric entry phase. When a space vehicle enters into a planet's atmosphere (Fig. 1.1), it reaches hypersonic regime and a strong shock is created in front of the body. This leads to a sharp increase of the temperature (and density) of the surrounding flow, typically up to 11000 K in the shock layer. The internal energy modes are progressively excited due to the rise of the translational temperature through the shock and molecules start to vibrate, dissociate and even ionize for sufficiently high temperatures. This creates a highly chemically reacting boundary layer and results in high heat-transfer rates to the spacecraft Thermal Protection System (TPS) [1]. The correct design of the heat shield is thus of utmost importance for the integrity of the vehicle and for the safety of the crew in case of manned mission.

Thermal Protection Systems categorization

When designing the heat shield of a spacecraft, one must not only know the peak heating sustained by the material, but also the integral over time of the heat flux during the entry

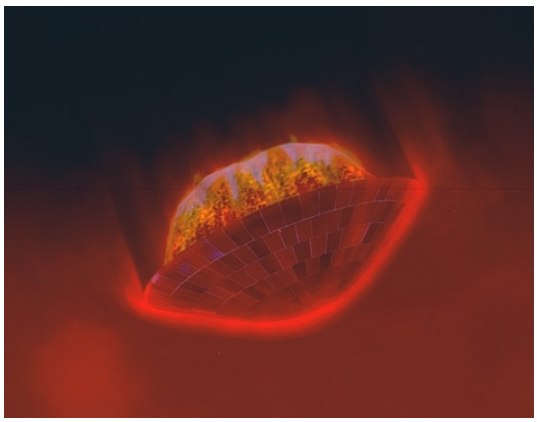

Figure 1.1: Artistic view of the Huygens Probe entry into Titan's atmosphere. Credit: ESA.

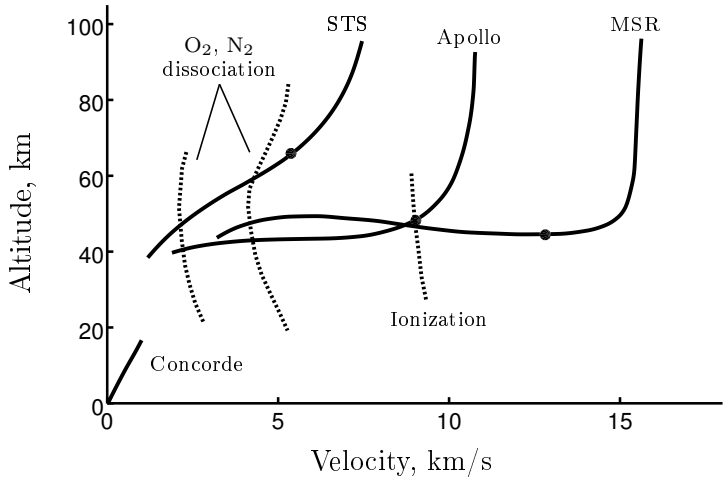

Figure 1.2: Reentry trajectories of the Space Shuttle (STS), Apollo capsule and Mars Sample Return (MSR) missions. The peak heatings are indicated by dots. Real gas effects as dissociation (more than 10% after the shock) and ionization are draw in dotted lines. Figure modified from Howe [16].

phase in order to correctly predict the TPS thickness. The different flight regimes are classically expressed under the form of a velocity-altitude map as shown in Fig. 1.2. For the comparison with a supersonic aircraft, the Concorde trajectory is also represented. During the reentry of missions such as sample return (e.g. MSR) or from extra-terrestrial return (Apollo), the speed at which the spacecraft arrived on Earth is very high (> 11 km/s). When it encounters the dense atmosphere of the Earth, the natural aerobraking generates very high heat fluxes that are transferred to the heat shield. On the other hand, for moderate velocity entries, such as for the Space Shuttle, the heat load on the spacecraft is lower.

Therefore, depending on the reentry conditions that are under consideration, the **type** of material used will be different. Thermal Protection Materials (TPMs) are classically divided in two main categories:

- **Ablative materials** (e.g. Apollo, MSL[1], Stardust[2], that lose mass when subjected to high thermal loads

- **Non-ablative materials**, or **reusable** TPSs, such as the ceramic tiles used for the Space Shuttle [37]. These materials re-radiate the incoming energy away from the surface of the TPS.

Ablative TPMs are generally used for entry speeds higher than 8 km/s and heat fluxes exceeding 1.5 MW/m^2 while reusable TPS are preferred for moderate speed entry, typically below 7.5 km/s and heat fluxes up to 1 MW/m^2. Only ablative materials are allowed to sustain the high heat fluxes encountered during high speed re-entries. These materials will therefore allow future sample return missions or planetary space exploration programs.

[1]Mars Science Laboratory. The entry capsule delivered successfully the Curosity Rover on 5 August 2012.

[2]Stardust. Collection of extra-terrestrial material from the coma of the comet Wild-2, February 1999 - January 2006

(a) Carbon preform material. (b) Carbon-phenolic material.

Figure 1.3: Examples of ablative material samples used for the thermal protection system of spacecraft. Credit: Airbus DS.

Ablative thermal protection materials

This work mainly focuses on ablative materials and will therefore be more detailed in the following sections. Ablative materials can be divided as well in two subcategories: **pyrolyzing** (or charring) and **non-pyrolyzing** materials. The name "pyrolysis" refers to the thermal degradation phenomenon that such material undergoes when subjected to elevated temperatures. Pyrolyzing materials are generally made of a polymeric resin matrix that binds together a network of more rigid carbon fibers. The resin absorbs the heat transmitted to the material and makes therefore these kind of material a more suitable choice for thermal protection systems. When heated, the resin sublimates and releases several gaseous species that percolate through the material. These pyrolysis gases add a blockage effect on the boundary layer gases reducing further the overall heating of the material by acting as a barrier against the incoming flow.

In the past, **dense** carbon/carbon and carbon/resin ablators have been used for many space applications (e.g. Apollo, Viking missions[3]) have showed the ability of such material to be used as heat shields. However lightness is an important issue for reducing the energy costs of propulsion and maximizing the payload of the entry vehicle, and yet TPSs must be strong enough to resist to spallation (mechanical ablation) and other possible mechanical failures of the material. These requirements led by the end of the 80's to the development of a new class of **low-density** carbon/phenolic materials, like the Phenolic Impregnated Carbon Ablator (PICA) by NASA [46] and later on, in 2008, to the development of Asterm by Airbus DS for ESA missions [40].

Two examples of low density thermal protection materials are showed in Fig. 1.3. The first material on Fig. 1.3a is made only of carbon fibers and is higly porous. Carbon-preform materials are generally not use directly for TPS but are mainly used as the building block for more complex carbon-phenol materials (1.3b). For the latter, the carbon fibers network is filled with a phenolic resin. Although filled with a resin content, carbon-phenolic materials are still highly porous.

The high mass efficiency and the low thermal conductivity of these low-density carbon/phenolic (pyrolyzing) materials explains the renewing interest in their development during the last decades. However, the use of such lightweight materials requires the modification and the adaptation of the previous models that were developed to study the former dense materials. Since then, these new materials have been under investigations and their experimental, as well as their numerical characterization, still need to be improved for a better optimization and design of heat shields.

[3] Viking 1 and Viking 2 probes were used to observe Mars from orbit and from surface. The two landers touched down the surface in July and September 1976.

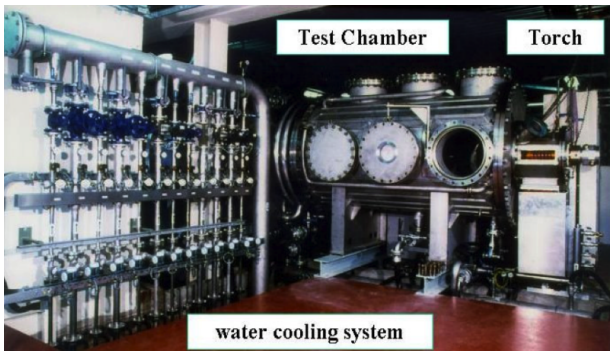

Figure 1.4: Photograph of the 1.2 MW Plasmatron wind tunnel. Credit: VKI.

State-of-the-art on material ablation studies

Experimental material response investigation

Real flight tests are seldom feasible and ground-based facilities are needed in order to reproduce the conditions characteristic of reentries. Ground-based facilities are therefore well-suited for the reproducibility of real flight experiments and allow the Thermal Protection Materials (TPMs) to be tested at a lower cost. However, a complete reproduction of the presented multiphysics reentry conditions in a single ground-based facility is not feasible and different types of wind-tunnels have been designed.

There exists two complementary strategies for ground tests used for studying high speed re-entry. On one hand, shock tubes are used to duplicate the shock layer and generate database for radiation features. On the other hand plasma wind tunnels duplicate the boundary layer around the vehicle and allow Gas Surface Interaction (GSI) investigations.

Plasmatron experiments for real flight conditions

In particular, the thermal response of TPMs are determined in plasma wind tunnels. The actual flight conditions can be related to the ones in plasma wind tunnels by means of a Local Heat Transfer Simulation (LHTS) methodology developed by Kolesnikov [18]. The experimental reproducibility of the heat transfer at the stagnation point is achieved ensuring similarity between enthalpy (or temperature), pressure and velocity gradient at the outer edge of the boundary layer. The VKI Plasmatron wind tunnel (Fig. 1.4) reproduces such high subsonic enthalpy flows and can provide dissociated flow for large characteristic times. The role of plasma winds tunnels is therefore to recreate the subsonic boundary layer close to the stagnation point in front of the hypersonic vehicle. The stagnation point is one the most critical part of the vehicle because it is often subjected to the highest heat fluxes and this point has been widely investigated in the past [2]. Recently, a large experimental test campaign in the VKI Plasmatron was performed by Herlber [13]. In particular, carbon preform and carbon-phenolic materials were both investigated.

Flow-tube experiments

An other type of facilities more dedicated to the material properties has also been developed. Past models for material ablation were assuming the recession to be only a surface phenomenon. This was mainly the case for high density material, but for low-density ablators different phenomena appear. Post-flight data analyses [45] as well as theoretical studies [19] showed that in-depth ablation was present in these highly porous materials.

The use of new leightweight porous ablators required therefore the development of new models to understand the physics of these materials and new facilities for validating these models needed to be developed.

This led to the design of an other type of facilities, dedicated to the testing of parameters and material properties. The flow-tube reactor at the NASA Ames Research Center was used by Panerai *et al.* to study the properties of carbon-preform material samples [38]. The competition between surface and volume ablation was observed on carbon preform in low-temperature, low-pressure regimes [38], showing that ablation was also a volume phenomenon. This volume ablation was shown to be a function of the Thiele number, or in other words, it is driven by the competition between diffusion and reaction inside the porous medium.

These experiments proved that an understanding of the behaviour at the microscopic scale was required for a good prediction of the material response. The importance of the coupling between the flow and the material was also emphasized and this will motivate the choice of the numerical approach for characterizing the material response, as explained in the next section.

Numerical material response investigation

Beside the development of ground test facilities, numerical codes have been developed as well for the prediction of the thermal response of TPMs, to help the design and the sizing of heat shields. The characterization of TPSs using numerical tools already started in the 60's but since then, many different codes have been developed. The common approaches for the numerical study of the response of ablative materials are mainly divided in three different methods, depending on how the problem is addressed.

Flow solver This first approach consists in solving the full Navier-Stokes equations and the chemistry in order to determine the loads on the TPS. Then the surface TPS is considered as a boundary condition which is determined by applying surface mass and energy balance at the wall. One example is the VKI stagnation line code [49].

Material response code This second approach rather consists in solving equations inside the material and applying again mass and energy balance at the surface. The first ablative material response code development already started in the late 1960's [17] with the CMA and ACE codes and most of the material response code developed after still rely on the same physical models. A short overview of the capabilities of different material codes is given in [20]. The different levels of modeling fidelity are presented and discussed.

These two first approaches can also be tightly coupled to improve the accuracy of the two methods by providing the boundary conditions to each code in an iterative way. For instance, the cote FIAT developed by Chen and Milos [6] is an upgrade of the CMA code and allows the coupling with the flow solver. However, the main issue with this approach remains in defining how and when boundary conditions are exchanged, leading naturally to the development of the last approach.

Unified flow-material code The third approach considered here consists in solving both the flow and the material in the same domain of computation, using equations that are valid everywhere (Fig. 1.5). Solutions for the different phases are obtained in a time accurate manner and there is no need anymore to exchange boundary conditions.

The first and the second approaches have been widely used in the past and are still in use nowadays. The first models developed were generally lacking of fidelity by neglecting many phenomena [17]. To compensate for the uncertainties in the analysis, large safety margin

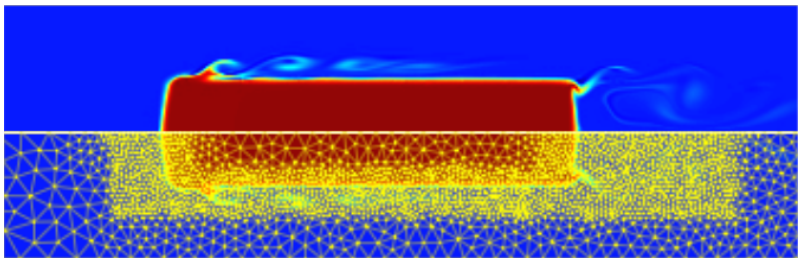

Figure 1.5: Numerical simulation of the ablation of a reactive porous medium using the unified approach. The material and the flow are in the same domain of computation and the mesh is represented in the bottom part. Credit: P. Schrooyen.

were added and increased the final weight of the TPS thus reducing the payload. Thanks to the improvements of computational capabilities and the development of new models, the fidelity of these codes was severely increased in the last decades. Many models considering phenomena as multispecies surface chemistry [34], spallation [36], volume ablation [19], water condensation [35], complex chemical-kinetic in the chemical boundary layer [39], are now proposed.

The last approach allows a better capture of the interactions of the flow with the material because both are solved in the same domain of computation. The numerical solver proposed by Dal Bianco *et al.* [9] follows this approach but considers the ablation as a surface phenomenon only and simplified equations for the material part are used. Finally, the code developed by Martin [32], based on the volume-averaged approach proposed by Lachaud *et al.* [19] to account for volume ablation, is accurate but Darcy's law momentum equation is solved and is adjusted to a fully developed laminar Poiseuille flow in the fluid region thus restricting the potential applications.

This work focuses on the third approach and uses the unified flow-material code developed by Schrooyen [42]. The numerical code, called DGAblation, is based on the Argo platform, a multi-physics code based on a discontinuous Galerkin method developed at Cenaero. The DGAblation module is solving the Volume Averaged Navier-Stokes (VANS) equations and allows to derive continuum relations for multiphase systems that are valid everywhere in the domain [51]. Thus, both the fluid and the material are solved in the same domain of computation. In his work, Schrooyen was able to reproduce the experiment of the NASA flow-tube facility from Panerai *et. al* using the numerical simulation tool Argo and the competition between surface and volume ablation was obersved [42].

Objectives and outline

The state-of-the-art of the computation of ablative materials response was presented as well as their experimental investigations. This project takes place at the center of these two fields. The experimental results available nowadays for material characterization allow the use of more accurate models requiring the development of high fidelity numerical codes. In this work, the attention is mainly devoted to the numerical study of low-density porous ablators, both pyrolyzing and non-pyrolyzing, by means of the unified flow-material solver Argo, introduced previously. The two main objectives of the project are now presented.

Objectives of the thesis

First objective: numerical simulation of the VKI Plasmatron experiments

The unique features of the unified flow-material solver allows to capture in an accurate manner the gas-surface interactions. Using this numerical tool, the first objective of this project to reproduce Plasmatron experiments on low-density carbon fibers materials. So far no multidimensional transient characterization of the surface and in-depth material response in Plasmatron experiments have been recreated numerically. Previously, the 1-D VKI stagnation-line code with a gas-surface interaction module to account for surface ablation was used to reproduce the experiments performed by Helber [49]. In the case of the present work, the whole experimental set-up of the Plasmatron will be simulated. The MUlticomponent Transport and Thermodynamic properties/chemistry for IONized gases (Mutation++) is used as a third party library to compute all chemistry and transport data [43].

Second objective: implementation and validation of a module for pyrolysis

Up to now, only non pyrolysing materials can be simulated by the numerical solver. A module for pyrolysis, although already present in many state-of-the-art numerical codes, still needs to be implemented and constitutes the second and the main part of this project. This second part therefore consists in the development of a module that accounts for the thermal degradation of carbon/phenolic-like material. The final steps are the verification on simple test cases of the new module and, finally, the reproduction of Plasmatron experiments on pyrolysing materials. This will be the first time, up to the author's knowledge, that a unified approach for flow-material, multidimensional and unsteady solver featuring material recession and pyrolysis will be developed.

Outline

This work is divided in six chapters. The first chapter is this short introduction presenting the main topic of the project.
In **Chapter 2**, the physical modeling of flow in porous medium is introduced. The contribution of the previous work of Schrooyen is presented. The contribution of this work is then described.
Chapter 3 presents briefly the numerical tool Argo used in this work. The basics of Discontiuous Garlekin (DG) methods for solving flow are presented.
In **Chapter 4** the experiments on carbon preform inside the Plasmatron are simulated used the numerical tool Argo.
Chapter 5 presents the test cases used to verify the newly implemented module that accounts for pyrolysis.
Finally in **Chapter 7** the conclusions of this work are drawn.

Chapter 2

Physical modelling

The atmospheric entry of a spacecraft is a particular case of hypersonic flows. There is no general rule to define hypersonic but it can be identified by the appearance of several complex multi-physics phenomena that are becoming dominant [1]. Those phenomena then influence strongly the behaviour of the flow around the spacecraft and the interaction with its surface.

This chapter presents the physical modeling of ablation in aerothermal entry problems. It is organized by increasing complexity of the problem. In the first section, hypersonic phenomena are briefly summarized and the physical setting of this work is defined.

The interaction of high temperature gas with the surface of the TPS is then described in Sec. 2.2. In particular, the pyrolysis phenomenon is emphasized as it is the main topic of the modeling section.

In the third section, the Navier-Stokes equations for multicomponent reactive flows are presented. As already stated, high-temperature gases are considered for our purpose in aerothermodynamics and the modelling of thermodynamics and transport properties of such flows are emphasized.

Low-density thermal protection materials are treated as porous media. The fourth section therefore introduces the modelling of flow in porous medium by means of Volume-Averaged Navier-Stokes (VANS) equations, which are an extension of the classir Navier-Stokes equations introduced in Sec. 2.3.

The last section finally consider the thermal degradation, or pyrolysis, of porous media. This corresponds for example to the particular case of resin-filled material used for heat shields of re-entry capsules. This last section constitutes the main contribution of this project to the previous work of Schrooyen [42].

Theoretical background in hypersonic re-entry flows

High-temperature gas effects

High-temperature gas effects are by far the most dominant ones in hypersonic. These are responsible of two typical mission killers during a spacecraft (re)entry that are the *gas-surface interaction* (GSI) and the *radiation*. The main outcome is the heating of the surface of the TPS, which is the result of different contributions.

The high viscous dissipation in the boundary layer (BL) can create very high temperatures. These strong temperatures are also generated due to the shock-layer, as stated in the introductory paragraph. The result is that the gas starts to vibrate, dissociate and even ionize (and thus is commonly referred as a *plasma flow*). Chemical reactions occur

inside the gas and the surface of the vehicle is covered by a *chemically-reacting boundary layer* that can interacts with the surface of the TPS.

The aerodynamic heating taking place from the hot boundary layer to the surface of the TPS is called *convective heating* and results in high heating transfer. Depending on the type of material used for the TPS, additional phenomena can occurs. Reusable TPS will absorb the incoming heat coming from the BL (convective and radiative heating, recombination) and will re-radiate it towards the gas. On the other hand, ablative TPSs will lose mass when heated caused by chemical reactions (oxidation, nitridation), or mechanical erosion. Generally ablative TPSs are filled with resin that also sublimates when subjected to high heat fluxes. Pyrolysis gases are released, adding more complexity to the interaction with the boundary layer gases.

When the temperature is high enough at the shock-layer edge, the gas can also emit radiation when going from an excited state to a less excited one, adding *radiative heating* to the surface. The importance of the radiation varies from one mission to the other. For low speed reentry, radiation heat flux is low but increases fast with velocity [10]. It also depends strongly on the atmosphere considered, as it was the case during the entry phase of the Huygens probe on Titan. The formation of CN species which is known to be a strong radiator was particularly dominant in that case [31]. However, the radiative heating from the hot gas will not be considered in this work.

Rarefied flow

At low altitude ($H < 80$ km) the flow is considered to be a continuum and this is the case for most of the practical aerodynamic applications. However, when growing with altitude, the air starts to be rarefied and the gas density is decreasing[1]. In order to understand the physics happening at higher altitudes ($H > 120$ km), the gas must be considered at the molecular level. The continuum description is based on the assumption that the mean free path λ (the average distance travelled by a single particle between two collisions) of the particles composing the gas is small compared to the characteristic length L of a given body. The validity of the continuum description is governed by the Knudsen number defined as the ratio between these two parameters

$$Kn = \frac{\lambda}{L}. \tag{2.1}$$

When considering rarefied, or free-molecular flow regimes, aerodynamics must be approached from a different point of view. Navier-Stokes equations are no longer valid and Botlzmann equation is used to described the evolution of the velocity of the particles in the gas and statistical mechanics is applied.

The free-molecular regime corresponds to the first part of the (re)entry phase of a space vehicle. Because there are less particles in the gas, the aerobraking and the heating of the spacecraft are low.

Hypotheses of this work

Following its reentry trajectory (Fig. 1.2), a spacecraft will generally encounter the different phenomena described in the previous sections[2]. In this work, flight conditions that

[1] For high altitude, the speed of sounds decreases leading to high value of Mach number and hypersonic regimes

[2] But also other phenomena not mentioned here, like the thickening of the boundary layer, or the creation of an entropy layer.

correspond to the last part of the trajectory are considered. The continuum assumption is made ($Kn < 0.1$) and the gas is characterized by a non-chemical equilibrium and thermal equilibrium. The question of the heat transfer in rarefied flow ($Kn > 10$) would require the modification of the approach of the problem (DSMC[3]. The radiation coming from the high temperature shock layer edge to the surface of the TPS is not considered here.

Gas surface interaction

The interaction of the carbon-resin composite materials used for the TPS with its surrounding environment is a very complex multi-physic phenomenon.

During the re-entry phase, a part of the heat flux is transferred inside the TPS, leading to a gradual temperature increase of the material. With this increase, large temperature gradients are establishing and the low density carbon/phenolic material is thermally degraded and removed by two physico-chemical phenomena: pyrolysis and ablation.

Pyrolysis-gas formation

In the pyrolysis zone, the polymeric resin[4] is thermally decomposed, losing mass while releasing pyrolysis gases under the form of water, hydrogen and hydrocarbons. This thermal degradation can be separated into three (overlapping) temperature regions characterized by the reactions occurring in each range [47], which may be described by four dominant heterogeneous reactions [48]. Trick and Saliba identified the different mechanisms occurring during pyrolysis using Fourier Transform Infrared Spectroscopy (FTIR) [47]. The kinetic parameters of the different reaction are then obtained by performing Thermogravimetry Analyses (TGA) and fitting the results to several Arrhenius laws [48].

The production of pyrolysis gas increases the internal pressure inside the sample. Lachaud *et al.* [23] showed numerically that these pressure gradients led to a flow that separates into two streams: one going toward the upper surface and blocking the gases from the boundary layer and one going toward the shoulder of an iso-flux sample.

Ablation process

The ablation of the char may be due to heterogeneous chemical reactions (oxidation, nitridation), phase change (sublimation) and/or mechanical erosion (spallation). Mechanisms of ablation depend on the re-entry conditions. For moderate temperature and pressure ($T < 3000$ K, $p < 55$ atm) [36], chemical ablation dominates. Most of the current ablation model consider that ablation is a surface phenomenon (all the mass is lost at the surface) [26, 27]. However, recent studies suggests that ablation of porous materials like PICA [45], should also occur in volume. Indeed, because of the high porosity of the material, reacting gas from the outer flow, mostly oxygen, diffuses inside the layer and reacts in the volume of the porous material with the carbon fibers. The key parameter for this in-depth ablation zone is the Thiele number [19, 42]

$$Th = \frac{L}{\sqrt{D_{eff}/S_f k_f}},$$

where D_{eff} is the effective diffusion inside the porous medium, S_f the specific surface and k_f is the reaction rate coefficient of the fibers. At high Thiele number, ablation is mostly

[3]Direct Simulation Monte-Carlo.

[4]Generally a phenolic resin like C_6H_5OH

a surface phenomenon because diffusion process is slow. Conversely, when diffusion is high enough and the reactivity relatively slow, the depth of the ablation zone becomes larger and volume ablation is promoted, leading to a low value of Thiele number.

After a short transient behaviour, four characteristic zones can therefore be distinguished:

- **Virgin zone:** region where the ablator is still in its virgin state and no pyrolysis gases exit yet from there.
- **Pyrolysis zone:** region where the pyrolysis reactions occur.
- **Char zone:** region where all the decomposable constituents from the resin have already been consumed. No more pyrolysis reaction can occur.
- **Ablation zone:** subregion of the char layer in which the ablation of the charred material is found to occur. Its thickness depends on Thiele number.

Sumamry of high-temperature gas effects

The Fig. 2.1 is a summary of the most dominant physical phenomena that have been mentioned so far. We consider at the top the shock layer, where dissociation and ionization of the species occur. Close to the surface of the TPS is the boundary layer. At the shock layer, species are dissociated while close to the surface of the material, where the temperature is lower, the species recombine. Diffusion occur between the shock layer and the boundary layer, as well as between the BL and the TPS. Note that no catalytic recombination is considered in this work.

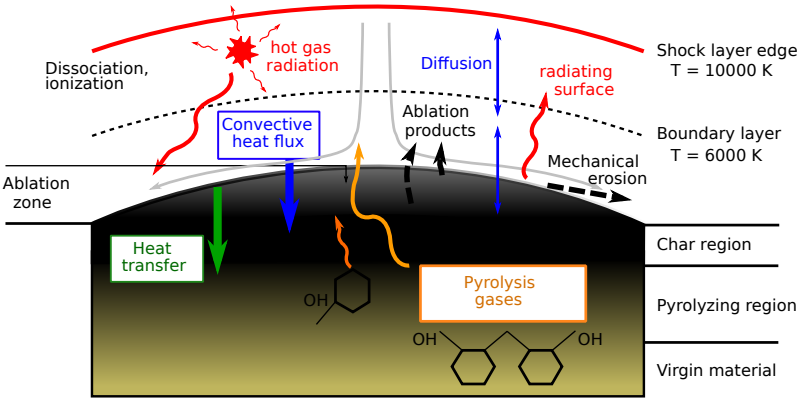

Figure 2.1: Summary of high temperature gas effects and gas surface interactions.

Heat is transferred to the material by convection, conduction and radiation from the hot gas. Pyrolysis gases are product in the pyrolysing region that percolate through the material towards the surface of the TPS. Material is removed by ablation that occur both at the surface and inside the material. Ablation products are produced and are ejected into the boundary layer. Additional charred material can be removed by mechanical erosion (spallation). All the phenomena mentioned here are considered in this work (except from the radiation of the hot gas and spallation). They need now to be described analytically by a set of equations that will be the topic of the next sections.

Gas-phase multicomponent reactive flows

Navier-Stokes equations

Mass, momentum and total energy conservation equations are written under the general formulation, in terms of conservative variables $\mathbf{U} = (\rho_i, \rho\boldsymbol{u}, \rho E)^T$

$$\frac{\partial \mathbf{U}}{\partial t} + \nabla \cdot \mathbb{F}^c = \nabla \cdot \mathbb{F}^d + \mathbf{S}, \tag{2.2}$$

where $\mathbb{F}^c$, $\mathbb{F}^d$ and $\mathbf{S}$ are respectively convective and diffusive fluxes and source term with

$$\mathbb{F}^c = \begin{pmatrix} \rho_i \boldsymbol{u} \\ \rho \boldsymbol{u} \otimes \boldsymbol{u} + P\overline{\overline{\boldsymbol{I}}} \\ \rho \boldsymbol{u} H \end{pmatrix}, \quad \mathbb{F}^d = \begin{pmatrix} -\boldsymbol{J}_i \\ \overline{\overline{\boldsymbol{\tau}}} \\ \overline{\overline{\boldsymbol{\tau}}} \cdot \boldsymbol{u} - \boldsymbol{q} \end{pmatrix}, \quad \mathbf{S} = \begin{pmatrix} \dot{\omega}_i \\ \mathbf{0} \\ \dot{\omega}_T \end{pmatrix}. \tag{2.3}$$

Many practical 3D applications can be expressed as 2D axisymmetric problems. Most of the test cases assumes that the flow is axisymmetric and in particular, the Plasmatron tests in which we are interested are generally described in cylindrical coordinates [29], [24]. Axisymmetry implies that derivatives in the θ direction cancel, $\partial \cdot / \partial\theta = 0$, and here azimuthal velocity u_θ is also neglected. A very useful formulation was implemented in Argo in which the 2D axisymmetric problem is expressed similarly to Eq. 2.2 and where only the source term is adapted in order to account for azimuthal components

$$\frac{\partial \mathbf{U}}{\partial t} + \left(\frac{\partial \mathbf{F}_x^c}{\partial x} + \frac{\partial \mathbf{F}_y^c}{\partial y} \right) = \left(\frac{\partial \mathbf{F}_x^d}{\partial x} + \frac{\partial \mathbf{F}_y^d}{\partial y} \right) + \mathbf{S} + \mathbf{S}^*, \tag{2.4}$$

where x and y stands now respectively for axial and radial directions. The term $\mathbf{S}^*$ is the only difference with the 2D cartesian development of Eq. 2.2. This additional source term is split in a convective and a diffusive contribution and is expressed as

$$\mathbf{S}^* = \mathbf{S}^c + \mathbf{S}^d = -\frac{1}{y} \begin{pmatrix} \rho_i u_x \\ \rho u_x u_y \\ \rho u_y^2 \\ \rho u_y H \end{pmatrix} + \frac{1}{y} \begin{pmatrix} 0 \\ \tau_{yx} \\ \tau_{yy} - \tau_{\theta\theta} \\ \tau_{yx} u_x - \tau_{yy} u_y - q_y \end{pmatrix}, \tag{2.5}$$

with $\tau_{\theta\theta}$ expressed by

$$\tau_{\theta\theta} = -\frac{2}{3}\mu \left(\frac{\partial u_x}{\partial x} + \frac{\partial u_y}{\partial y} - 2\frac{u_y}{y} \right). \tag{2.6}$$

Flow in non-pyrolysing reactive porous media

The flow and the material regions are considered together in the same domain of computation. The previous Navier-Stokes equations are valid only in the fluid region and a set of equation valid in both domains is required. Solving the equations of transport inside the pores would be impossible because of the large differences in length scales. Therefore, an extension to mutli-phase flow is sought here by performing local volume averaging operations on the initial set of equations [51]. This approach of smoothing a set of equations valid in one phase is now introduced in this section. Volume-Averaged Navier-Stokes equations valid for compressible multi-species and reactive flows are briefly described here. A complete derivation of this new set of equations is out of the scope of this thesis but more extensive explanations can be found in [42]. This section focus mainly on the modelling of preform materials made only of carbon fibers and describes the work performed by Schrooyen on solving multi-phase flow for ablation problem in Argo.

Local volume averaging

The equations describing one phase are averaged over a small Representative Elementary Volume (REV), as sketched in Fig. 2.2. The continuum hypothesis inside the pores, described by the local Knudsen number, is assumed to be valid towards this work and the continuum equations are valid. The superficial average operator on a quantity α is

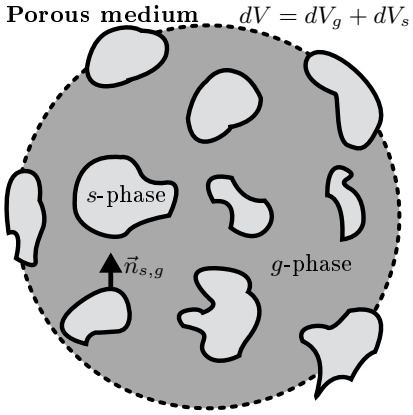

Figure 2.2: Sketch of a Represetative Elementary Volume (REV) on which local volume averaging is performed.

introduced

$$\langle \alpha \rangle = \frac{1}{dV} \int_{dV} \alpha dv. \tag{2.7}$$

Denoting a general phase γ, the intrinsic average is defined as

$$\langle \alpha \rangle_\gamma = \frac{1}{dV_\gamma} \int_{dV_\gamma} \alpha dv, \tag{2.8}$$

where the averaging operation is performed only on the phase considered. dV_γ represents the volume of the γ phase inside the whole REV dV. Volume fractions are introduced as the fraction of a γ phase over the entire volume

$$\varepsilon_\gamma = \frac{dV_\gamma}{dV}. \tag{2.9}$$

Superficial and intrinsic averaged are link together by means of the volume fraction

$$\langle \alpha \rangle = \varepsilon_\gamma \langle \alpha \rangle_\gamma \tag{2.10}$$

For our purpose here of a fluid and solid phases, the term *porosity* (ε_g) is used to denote the fluid fraction

$$\varepsilon_g = \frac{dV_g}{dV}, \quad \varepsilon_s = 1 - \varepsilon_g = \frac{dV_s}{dV} \tag{2.11}$$

and ε_s is the solid fraction.

Volume-Averaged Navier-Stokes equations

Applying the local average operators Eqs. 2.7 and 2.8 to the classical set of Navier-Stokes equations (2.2), Volume-Averaged Navier-Stokes equations that are valid in both fluid phase are derived. These equations are summarized below and their main assumptions are stated.

Species mass conservation

Mass conservation equation for a gaseous species i reads

$$\frac{\partial(\varepsilon_g\langle\rho_i\rangle_g)}{\partial t} + \nabla\cdot(\varepsilon_g\langle\rho_i\rangle_g\langle\boldsymbol{u}\rangle_g) = -\nabla\cdot\langle\boldsymbol{J_i}\rangle + \langle\dot{\omega}_i^{hom}\rangle + \langle\dot{\omega}_i^{het}\rangle. \tag{2.12}$$

Heterogeneous chemical reactions of the fluid species i with the solid surface are denoted by $\dot{\omega}_i^{het}$. These reactions are modelled using first order irreversible reactions

$$\dot{\omega}_i^{het} = S_f k_f^i \langle\rho_i\rangle_g, \tag{2.13}$$

where S_f is the specific surface of the fibers, that will be developed later on in Sec. 2.4.3, k_f^i is the forward rate of reaction of species i with the fibers and $\langle\rho_i\rangle_g$ the average species density. Diffusive fluxes are given by

$$\langle\boldsymbol{J_i}\rangle = -\varepsilon_g\langle\rho_i\rangle\frac{D_{i,m}}{\eta}\frac{W_i}{W}\nabla X_i + \varepsilon_g\langle\rho_i\rangle_g\sum_{k=1}^{N_s}\frac{D_{k,m}}{\eta}\frac{W_k}{W}\nabla X_k \tag{2.14}$$

where the effective diffusion is defined as

$$D_{eff} = \frac{\varepsilon_g}{\eta}D_{i,m} \tag{2.15}$$

in which the tortuosity η is introduced and need to be modelled for the closure of the equation. Tortuosity depends on the porosity and a linear interpolation between plain fluid tortuosity ($\eta = 1$) and the initial porous medium tortuosity ($\eta = \eta_0$) is used to describe their correlation,

$$\eta = \frac{1-\eta_0}{1-\varepsilon_{g,0}}(\varepsilon_g - 1) + 1. \tag{2.16}$$

Momentum conservation law

The volume-averaged momentum equation reads

$$\frac{\partial(\langle\rho\boldsymbol{u}\rangle_g)}{\partial t} + \nabla\cdot(\langle\rho\rangle_g\langle\boldsymbol{u}\rangle_g\langle\boldsymbol{u}\rangle_g = \varepsilon_g\nabla\langle P\rangle_g + \nabla\cdot\langle\overline{\overline{\boldsymbol{\tau}}}\rangle + \frac{\mu}{\kappa}\varepsilon_g^2\langle\boldsymbol{u}\rangle_g, \tag{2.17}$$

where κ is the permeability of the medium. It's a parameter that depends on the microstructure of the medium and measure the ability of a fluid to flow though the porous material. The permeability evolves with porosity and different laws can be expressed to approximate its evolution. In this work, the semi-heuristic model of Carman-Kozeny is used

$$\kappa^{-1} = \frac{S_{f,0}^2(1-\varepsilon_g)^2 k_k}{\varepsilon_g^3}, \tag{2.18}$$

where $S_{f,0}$ is the initial specific surface and k_k is a constant directly proportional to the tortuosity. A linear relation is also used, where

$$\kappa^{-1} = \frac{1}{\kappa_0}\frac{(1-\varepsilon_g)}{\varepsilon_{s,0}}. \tag{2.19}$$

The differences between the different permeability model, as well as their influence on several test cases, was investigated by Schrooyen [42].

Energy conservation law

Energy conservation law reads

$$\frac{\langle \rho E_{tot} \rangle}{\partial t} = \nabla \cdot (\varepsilon_g \langle \rho \rangle_g \langle H \rangle_g \langle \boldsymbol{u} \rangle_g) = \nabla \cdot (\lambda_{eff} \nabla T) + \nabla \cdot (\langle \overline{\overline{\boldsymbol{\tau}}} \cdot \boldsymbol{u} \rangle) - \nabla \cdot \left(\langle \sum_i^{N_s} J_i h_i \rangle \right) \tag{2.20}$$

The effective conductivity λ_{eff} is modelled as an first approximation as a average between solid conductivity and fluid thermal conductivity, weighted by their respective volume fraction as

$$\lambda_{eff} = \varepsilon_s \lambda_s + \varepsilon_g \lambda_g. \tag{2.21}$$

Solid mass equation

When surface recession is tracked (variable porosity), one additional variable need to be specified to account for the variation of solid density, which are the fibers $\langle \rho_f \rangle$. The fibers are only degraded by chemical reactions and in order to account for this degradation, the sum over all production rate of species i is performed. Solid mass conservation equation reads

$$\partial_t \left(\varepsilon_s \langle \rho_s \rangle_s \right) = - \sum_{i=1}^{N_{sr}} \dot{\omega}_{het} = - \sum_{i=1}^{N_{sr}} S_f k_f^i \langle \rho_i \rangle_g \tag{2.22}$$

where N_{sr} denotes the number of reactions occurring with the solid.

Fibers recession

The process of averaging the equations lays out in the new system of equations parameters that render the microstructure of the porous medium. On one hand a level of abstraction is added to the problem and avoid the resolution of all length scales, but on the other hand new closure models are required.

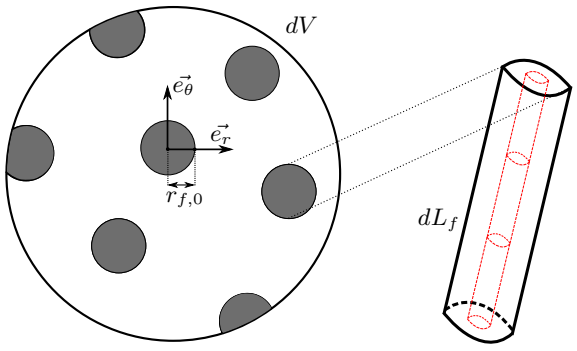

Figure 2.3: Simplified model for porous medium with cylindrical fibers.

The heterogeneous reactions are assumed to be irreversible first order reaction between the solid phase and the fluid phase. The heterogeneous production term is

$$\langle \dot{\omega}_{het} \rangle = -S_f k_f \langle \rho_i \rangle_g, \tag{2.23}$$

where k_f is the forward reaction rate, $\langle \rho_i \rangle_g$ is the intrinsic density of a reactant i and S_f is the specific surface. The latter one is defined as the surface dA_w of the solid phase which is in contact with the gas phase in the elementary volume dV

$$S_f = \frac{dA_w}{dV} \tag{2.24}$$

Considering N_f fibers of length dL_f in the control volume $dV = dV_s/\varepsilon_s$, it follows for the cylindric-shaped fibers

$$\begin{aligned} S_f &= \frac{2\pi r dL_f N_f}{dV_s}\varepsilon_s \\ &= \frac{2\pi r dL_f N_f}{\pi r^2 dL_f N_f}.\varepsilon_s \end{aligned} \tag{2.25}$$

The radius of the fibers can be expressed as a function of the initial fiber radius $r_{f,0}^2$ and solid volume fraction $\varepsilon_{s,0}$ as

$$\frac{\varepsilon_s}{\varepsilon_{s,0}} = \frac{r^2}{r_{f,0}^2} \tag{2.26}$$

The specific surface for the cylindrical model is finally given by

$$S_f = \frac{2}{r_{f,0}}\sqrt{\varepsilon_{s,0}\varepsilon_s}. \tag{2.27}$$

A sinusoidal model was also implemented by Schrooyen [42] in order to model the phenomenon of pitting. It allows to account for an increase of the specific surface due to the formation on holes on the fibers observed in some cases [13]. However this model is not considered here and the specific surface is assumed to increase as the square root of the solid fraction as expressed by Eq. 2.27.

Flow in pyrolysing reactive porous media

In the previous section, VANS equations were introduced. These equations are used to solve flow in porous media and a model accounting for oxidation of solid fibers was presented. The treatment of low-density reactive porous materials made of several solid phases is now addressed.

This last section describes the model for pyrolyzing material that was implemented inside the numerical solver. The implementation of state-of-the art models accounting for the thermal degradation and charred oxidation of an ablative composite material inside the numerical tool Argo (see Chap. 3) constitutes the main contribution of this work to the solver. Attention is focus of carbon-phenolic materials dedicated to the integration in thermal protection systems like PICA or Asterm.

Model for Pyrolysis

The solid medium is considered to be made of fibers with a resin filling matrix in between them. The average solid density is expressed as the sum of the two average densities

$$\langle \rho_s \rangle = \langle \rho_f \rangle + \langle \rho_m \rangle \tag{2.28}$$

where the subscript f denotes the fibers and m the matrix. It can be defined in terms of intrinsic solid densities as

$$\varepsilon_s\langle\rho_s\rangle_s = \varepsilon_f\langle\rho_f\rangle_f + \varepsilon_m\langle\rho_m\rangle_m \tag{2.29}$$

where ε_f and ε_m denote the fibers and matrix fractions respectively. The solid mass conservation equation 2.22 now reads

$$\partial_t\left(\varepsilon_f\langle\rho_f\rangle_f + \varepsilon_m\langle\rho_m\rangle_m\right) = \dot{\omega}_{het} + \dot{\omega}^{pyro} \tag{2.30}$$

Goldstein showed by means of thermogravimetric measurements [12] two maximum in rate of weight loss for the phenolic resin, suggesting that the pyrolysis of the resin takes place in two major reactions (A and B). The volume-averaged matrix density can be expressed as the sum of two fake resin components

$$\langle\rho_m\rangle = \langle\rho_{m,A}\rangle + \langle\rho_{m,B}\rangle \tag{2.31}$$

that will decompose at different rate of reactions. For a general N step decomposition process, average matrix density writes

$$\langle\rho_m\rangle = \sum_{I=A}^{N}\langle\rho_{m,I}\rangle. \tag{2.32}$$

The rate of decomposition of each resin compounds are expressed by using several Arrhenius type law

$$\partial_t\langle\rho_{m,I}\rangle = -A_{0,I}\langle\rho_m^v\rangle\exp\left(\frac{-Ea_I T}{\mathcal{R}}\right)\left(\frac{\langle\rho_{m,I}^v\rangle - \langle\rho_{m,I}^c\rangle}{\langle\rho_{m,I}^v\rangle}\right)^{n_I} \tag{2.33}$$

where $A_{0,I}$ is the specific reaction constant (s^{-1}), Ea_I is the Arrhenius activation energy (J/mol), $\mathcal{R}$ the universal gas constant (J/mol-K), n_I the reaction order, $\langle\rho_m^v\rangle$ the initial averaged density of the virgin matrix, $\langle\rho_{m,I}^v\rangle$ and $\langle\rho_{m,I}^v\rangle$ the initial virgin and char density of the resin compounds I. Virgin and char average resin species densities express as

$$\langle\rho_{m,I}^v\rangle = F_I^v\langle\rho_m^v\rangle \tag{2.34}$$

$$\langle\rho_{m,I}^c\rangle = F_I^c\langle\rho_m^c\rangle \tag{2.35}$$

where F_I^v and F_I^c are defined as the fraction of virgin and char matrix corresponding to the fake species I.

As several pyrolysing processes are considered, a progress variable for each local pyrolysis reaction is introduced

$$\xi_I = \frac{\langle\rho_{m,I}^v\rangle - \langle\rho_{m,I}\rangle}{\langle\rho_{m,I}^v\rangle - \langle\rho_{m,I}^c\rangle} \tag{2.36}$$

and the global advancement of reaction expresses as a linear combination of the local ones

$$\xi = \sum_I F_I^v\xi_I. \tag{2.37}$$

The production term in Eq. 2.30 is decomposed between a contribution from the heterogeneous reactions with the fibers and a contribution coming from the resin decomposition of each solid species $\dot{\omega}_p = \dot{\omega}_{het} + \dot{\omega}^{pyro}$. The rate of resin decomposition is therefore

$$\dot{\omega}^{pyro} = \sum_I \partial_t\langle\rho_{m,I}\rangle \tag{2.38}$$

Charred material modeling

The resin binders is thermally degraded and progressively transformed into a low-density carbon residue, forming with the carbon fibers what is called the charred material.

As a first approximation, the reactivity of the charred material is assumed to be the same as the one of the fibers, i.e. $k_m = k_f$. However it should be kept in mind that the reactivity of the carbonized matrix is theoretically higher. The structure of the matrix includes many more defects that the carbon fibers and a second estimation of the reactivity could be for instance $k_m = 10k_f$ [19].

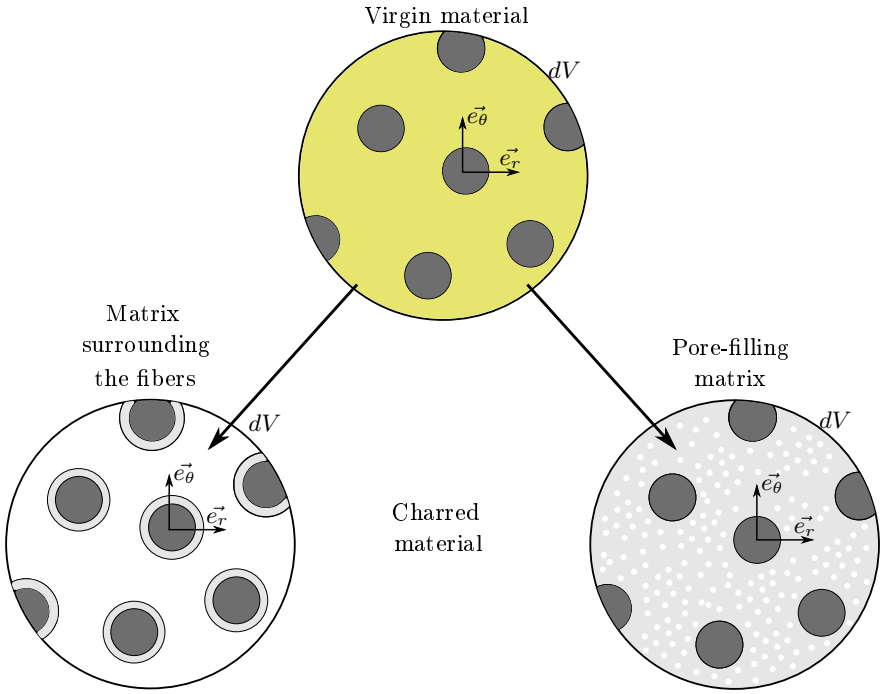

Figure 2.4: Illustration of the different models for charred material.

Matrix surrounding the fibers

Considering the previous model for carbon fibers recession, a model of char surrouding the fibers as sketched in Fig. 2.4 (left) is the most straightforward to adapt. An equivalent fibers radius is defined

$$r_e = r_{f,0} + e_c \tag{2.39}$$

where e_c denotes the char thickness.

$$r_e = r_{f,0}\sqrt{\frac{\varepsilon_s}{\varepsilon_{f,0}}} \tag{2.40}$$

which has exactly the same formulation as the previous radius defined in Eq. 2.26[5], except that now the equivalent radius can have values bigger than the initial fiber radius $r_{f,0}$. Following the same development as before, the specific surface is defined as

$$S_f = \frac{2}{r_{f,0}}\sqrt{\varepsilon_{f,0}\varepsilon_s} \tag{2.41}$$

which is valid both for charred and preform material.

[5]Note that in (2.26) the solid fraction is equal to the fibers fraction

Pore-filling matrix

The other way round is to consider that the matrix is not located around the fibers but is still filling the void between the fibers as for the resin, as sketched in Fig. 2.4 (right). The specific surface S_f is a function of the matrix fraction ε_m, that can be as simple as a linear relation. This functional relation that depends on the topology of the medium is not well known and experiments on the carbonized matrix would be needed to estimate this dependency [19]. A functional that evolves as the square root of the matrix fraction is equivalent to the model of the matrix surrounding the fibers described previously.

The model of the matrix surrounding the fibers is first implemented in the Argo code. In future work, it could be interesting to investigate the influence of the model of the charred material on the ablation of the porous medium by playing with the functional dependence of the specific surface.

Volume-averaged Navier-Stokes equations

Energy conservation law

The total energy $\langle \rho E_{tot} \rangle$ is composed of the energy of the fluid phase, in which kinetic energy is accounted, and the energy of the static solid phase

$$\langle \rho E_{tot} \rangle = \varepsilon_g \left[\langle \rho \rangle_g \left(\langle e \rangle_g + \frac{\langle \boldsymbol{u} \rangle_g^2}{2} \right) \right] + \varepsilon_s \langle \rho \rangle_s \langle e \rangle_s. \tag{2.42}$$

Because now the solid is composed of the fibers and the matrix, we have

$$\varepsilon_s \langle \rho \rangle_s \langle e \rangle_s = \varepsilon_f \langle \rho \rangle_f \langle e \rangle_f + \varepsilon_m \langle \rho \rangle_m \langle e \rangle_m. \tag{2.43}$$

Summary of the equations

Recalling the compact form of the system of equations

$$\frac{\partial \mathbf{U}}{\partial t} + \nabla \cdot \mathbb{F}^c = \nabla \cdot \mathbb{F}^d + \mathbf{S}, \tag{2.44}$$

The set of conservative variables for the Volume-averaged Navier-Stokes equations is now

$$\mathbf{U} = \begin{pmatrix} \varepsilon_g \langle \rho_i \rangle_g \\ \langle \rho \boldsymbol{u} \rangle_g \\ \langle \rho E_{tot} \rangle \\ \langle \rho_f \rangle \\ \langle \rho_I \rangle \end{pmatrix}, \tag{2.45}$$

The convective and diffusive fluxes express as

$$\mathbb{F}^c = \begin{pmatrix} \varepsilon_g \langle \rho_i \rangle_g \langle \boldsymbol{u} \rangle_g \\ \langle \rho \rangle_g \langle \boldsymbol{u} \rangle_g \langle \boldsymbol{u} \rangle_g + P \\ \varepsilon_g \langle \rho \rangle_g \langle \boldsymbol{u} \rangle_g \langle H \rangle_g \\ \mathbf{0} \\ \mathbf{0} \end{pmatrix}, \qquad \mathbb{F}^d = \begin{pmatrix} -\langle \boldsymbol{J_i} \rangle \\ \langle \overline{\overline{\boldsymbol{\tau}}} \rangle_g \\ \langle \overline{\overline{\boldsymbol{\tau}}} \cdot \boldsymbol{u} \rangle + \lambda_{eff} \nabla \langle T \rangle - \sum_{i=1}^{N_s} h_i \langle \boldsymbol{J_i} \rangle \\ \mathbf{0} \\ \mathbf{0} \end{pmatrix}. \tag{2.46}$$

Finally, the source term is

$$\mathbf{S} = \begin{pmatrix} \langle \dot{\omega}_i^{het} \left(\langle T \rangle, \langle \rho_i \rangle_g, \langle \rho_s \rangle \right) \rangle + \varepsilon_g \dot{\omega}^{hom} \left(\langle T \rangle, \langle \rho_i \rangle_g \right) + \langle \dot{\omega}_I^{het} \left(\langle T \rangle, \langle \rho_I \rangle \right) \rangle \\ \boldsymbol{F_{gs}} \\ -\sum_{i=1}^{N_s} \left(\langle \dot{\omega}_i^{het} \left(\langle T \rangle, \langle \rho_i \rangle_g, \langle \rho_s \rangle \right) \rangle + \varepsilon_g \dot{\omega}^{hom} \left(\langle T \rangle, \langle \rho_i \rangle_g \right) \right) h_{f,i}^0 \ \cdots \\ -\sum_{I=1}^{N_p} \left(\langle \dot{\omega}_I^{het} \left(\langle T \rangle, \langle \rho_I \rangle \right) \rangle h_{f,I}^0 + \sum_{j=1}^{N_s} \langle \omega_{j,I}^{het} \left(\langle T \rangle, \langle \rho_I \rangle \right) \rangle h_{f,j}^0 \right) \\ \sum_{i=1}^{N_s} \langle \dot{\omega}_i^{het} \left(\langle T \rangle, \langle \rho_i \rangle_g, \langle \rho_s \rangle \right) \rangle \\ \sum_{I=1}^{N_p} \langle \dot{\omega}_I^{het} \left(\langle T \rangle, \langle \rho_I \rangle \right) \rangle \end{pmatrix}. \tag{2.47}$$

Review of the chapter

In this chapter, we discussed the different physical phenomena encountered during the (re)-entry phase of a spacecraft and the need for developing new model for the decomposition of the thermal protection system was emphasized. In particular, the Volume-Averaged Navier-Stokes equations have been presented. This set of equations is valid over the whole domain and allows to solve the ablation phenomenon of a porous medium made of fibers. A set of different properties coming from the smoothing of the equation and reflecting the microstructure of the porous medium was introduced and model for these properties is needed.

The treatment of several solid phases inside the porous medium was also presented. Additional solid mass conservation equations are added to the previous one. A two rate decomposition law that comes from thermogravimetric analyses is chosen to model the decomposition of a pyrolyzing material. Once the material has pyrolyzed at one specific location, the charred material is assumed to surround the fibers and a cylindrical model for the recession of the carbonized matrix is assumed.

Chapter 3

Computational modelling

EQUATIONS for modelling multi-phase flows, accounting for fibers recession and thermal degradation of a porous medium have been presented in Chap. 2. This set of equations now need to be solved numerically and the presentation of the numerical techniques is the purpose of this chapter. As already mentioned earlier, the numerical tool Argo which implements a Discontinuous Galerkin (DG) discretization is used towards the whole project. Discontinuous Galerkin Method was first proposed in the early 70s but up to now is not very common in the field of CFD. Some attention is therefore paid to the method and its implementation in the Argo solver. The solver is first introduced and briefly presented in Sec. 3.1. The spatial and the temporal discretization are then discussed in Sec. 3.2 and Sec. 3.3 respectively and the implementation of the boundary conditions within the code are presented in Sec. 3.2.4. A lot of different discretization schemes are available inside Argo, with various rate of convergence, levels of complexity and properties to solve some specific problems. However it is not the intend to this introductory chapter to cover all of them and we will focus on the ones that are mainly used.

During this thesis, the approximation methods and discretization schemes were not modified. The resolution of the new set of equations implemented within Argo relies strictly on the numerical schemes already implemented, thanks to the polymorphism of the interface. This makes Argo a suitable choice for the study of aerothermal flows as we are benefiting from the results of several years of research in multi-physics CFD and in DGM [14, 5, 42]. The intend of this chapter is therefore to give a rapid overview of the solver and its main features.

Argo: a high-order numerical tool

Argo is a multi-physics and multi-dimensional platform implementing a Discontinuous Garlekin Method (DGM). It is currently developed at Cenaero (Gosselies, Belgium) and involves several full-time researchers, making the solver continuously tested and improved. The code is written in C++ and allows to add easily new conservation laws to the previous ones. It is also featuring a hybrid Message Passing Interface (MPI) and Open-Multi-Processing (OpenMP) for the parallelization.

The platform includes several modules that can solve a large variety of flows, ranging from simple incompressible, compressible or acoustic problems up to the simulation of turbulent flows and multiphase flows. The latest module integrated to the platform was the *DGAblation* interface [42] that allows to solve ablation problems. An interface with the library MUTATION++ was also added to the module allowing the computation of accurate

transport and thermodynamic properties to be used when dealing with aerothermal flows. The *DGAblation* module is the one that is under investigation and was complemented throughout this project.

Space discretization

This section cover the basic of the Discontinuous Galerkin method. Its implementation to CFD is described and the main advantages are discussed.

Discontinuous Galerkin method

DGM is a mix between Finite Element and Finite Volume Methods (FEM and FVM), and therefore combines the advantages of both methods. It allows to obtain an arbitrary high order of convergence on unstructured meshes. The locality of the data and operations arising from the piecewise finite elements allow also a very efficient scalability of the problem on parallel machines.

The main idea of the Discontinuous Galerkin Method is the reinterpretation of the Classical Galerkin Finite Element Method (CGFEM) as a combination of element-wise finite element problem coupled with internal boundary conditions.

The system of equation 2.44 is rewritten as

$$\mathcal{L}_m(\widetilde{\mathbf{u}}) = 0, \quad \forall m \in \{1, N_v\} \tag{3.1}$$

$$= \frac{\partial \widetilde{u}_m}{\partial t} + \frac{\partial}{\partial x^k} F_m^{c,k}(\widetilde{\boldsymbol{u}}) - \frac{\partial}{\partial x^k} F_m^{d,k}(\widetilde{\boldsymbol{u}}, \nabla \widetilde{\boldsymbol{u}}) - S(\widetilde{\boldsymbol{u}}, \nabla \widetilde{\boldsymbol{u}}), \tag{3.2}$$

The diffusion term is the following is expressed using the Jacibian of the diffusive flux with respect to the solution gradients defined as

$$F_m^{d,k} \approx -D_{m,n}^{k,l}(\boldsymbol{u}) \frac{\partial \widetilde{\boldsymbol{u}}_n}{\partial x^l}, \tag{3.3}$$

where $D_{m,n}^{k,l}$ is a fourth order tensor relating the diffusive flux for variables m and in direction k and where Einstein summation applies on the dummy index l. The objective is to derive a weak formulation of the system of equations.

Weak formulation

A weak formulation of the set of Partial Differential Equations, valid locally, is obtained by multiplying them by a test function define on the functional test space $mathcalV$, and integrating the result over an arbitrary volume. Applying to the non linear operator of the VANS equations, it follows

$$\int_\Omega v \mathcal{L}_m(\boldsymbol{u}) = 0, \quad \forall v \in \mathcal{V} \tag{3.4}$$

Galerkin approximation

So far the weak formulation (3.4) is strictly equivalent to the strong from described by the PDEs as no approximation has been made. As in CGFEM, the approximation of the solution then relies on the form of the function used for the elements. Finite element methods are widely used in structural mechanics in order to solve complex problem of elasticity. The solution at the interface between two elements is therefore imposed to be

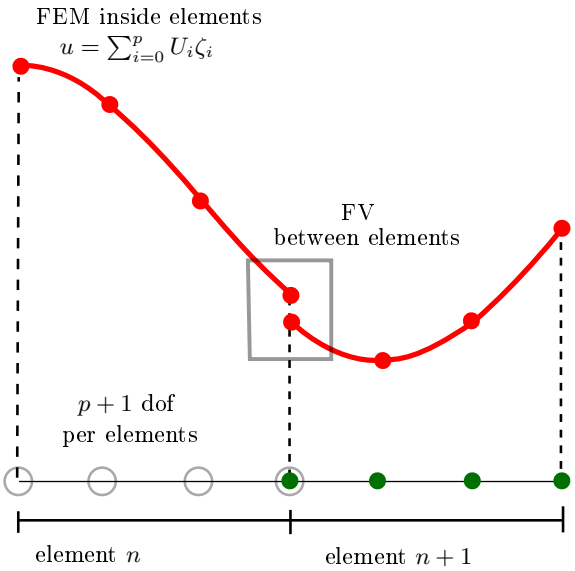

Figure 3.1: Representation of two elements in the Dinscontinuous Galerkin disctretization using third order Langrangian polynomial interpolation in 1D. Figure reproduces from [42].

continuous. In the DGM and as in all CGFEM, the domain (Ω) is decomposed in a set of finite element (Ω_e) that covers the entire domain without overlapping. The approximate solution is expressed as a linear combination of the shape functions ζ_i on each element

$$\widetilde{u}_m \approx u_m = \sum_{i=1}^{N} U_{i,m} \zeta_i, \tag{3.5}$$

where the coefficient $U_{i,m}$ are the DOFs of the problem and N the number of element Ω_e in the domain. In general, elements are also allow to have different shape functions, allowing the solution to be written as

$$u_m = \sum_{e} \sum_{i=1}^{N^e} U^e_{i,m} \zeta^e_i \tag{3.6}$$

The main difference with the DGM lies in the interface that is no longer assumed to be continuous and the discretization of the weak formulation is now presented.

Discontinuous Galerkin approximation applied to the convection-diffusion-reaction problem

By applying partial integration to the weak formulation Eq. 3.4 and applying the Galerkin approximation, the approximation of the weak formulation reads [42]

$$
\begin{aligned}
\int_\Omega v\mathcal{L}_m(u) &= 0, \quad \forall v \in \mathcal{V}, \quad \forall m \in N_v \\
&= \underbrace{\sum_{\Omega_e \in \Omega} \int_{\Omega_e} v \frac{\partial u_m}{\partial t} d\Omega_e}_{T_v} \\
&\underbrace{- \sum_{\Omega_e \in \Omega} \int_{\Omega_e} \frac{\partial v}{\partial x^k} F_m^{c,k}(\boldsymbol{u}) d\Omega_e}_{C_v} + \underbrace{\sum_{I_i \in I} \oint_{I_i} [v]^k \, n^k \mathcal{H}_m(\boldsymbol{u}^+, \boldsymbol{u}^-, \boldsymbol{n}) dS}_{C_i} \\
&\underbrace{+ \sum_{\Omega_e \in \Omega} \int_{\Omega_e} \frac{\partial v}{x^k} (F_m^{d,k}(\boldsymbol{u})) d\Omega_e}_{D_v} \underbrace{- \sum_{I_i \in I} \oint_{I_i} \langle D_{mn}^{kl} \frac{\partial \boldsymbol{u_n}}{\partial x^l} \rangle \, [v]^k \, dS}_{D_i} \\
&\underbrace{- \theta \sum_{I_i \in I} \oint_{I_i} \langle D_{mn}^{kl} \frac{\partial v}{\partial x^l} \rangle \, [u_m]^k \, dS}_{D_t} \underbrace{+ \alpha \sum_{I_i \in I} \oint_{I_i} [v]^k \, [u_m]^k \, dS}_{D_p} \\
&\underbrace{- \sum_{\Omega_e \in \Omega} \int_{\Omega_e} v S(\boldsymbol{u}, \nabla \boldsymbol{u}) d\Omega_e}_{S_v}
\end{aligned}
\tag{3.7}
$$

In the equation above, the Einstein notation applied on dummy index. Jump and average trace operators are defined respectively by

$$[a] = a^- n^- + a^+ n^+ \tag{3.8}$$

$$\langle a \rangle = \frac{1}{2}(a^- + a^+) \tag{3.9}$$

The temporal term is noted T_v. The terms C_v, D_v and S_v are the volume contributions of the convective, diffusive and source terms respectively. These terms are common to both CGFEM and DGM. The terms C_i, D_i, D_t and D_p can be considered as internal boundary conditions that couple and element with its neighbors as in FVM. Convective, diffusive terms and interfaces fluxes are now briefly discussed.

Convective variational terms

Discontinuous Galerkin approximation of the convective variational terms was shown to be an extension of finite volume method to high order approximations [14]. The previous formulation of the discretization of the convective variational terms takes its inspiration from upwind fluxes.

Interface fluxes

The discretization of the convective terms always involves the resolution of a Riemann problem. Energy stability can be obtained by using upwind fluxes. Within Argo, several

Table 3.1: Main boundary conditions implemented in Argo. The superscript "+" denotes interior values while "−" denotes outer values. $\mathbf{U}$ is the set of conservative variables and the diffuse fluxes are denotes $\mathbf{F}^d$. Table reproduced from Schrooyen [42].

Boundary type	Euler Conditions	NS Conditions
Subsonic inflow	$\boldsymbol{u}^-, T^-, Y_i$ are given and $P^+ = P^-$	$\mathbf{F}^{d,+} \cdot \mathbf{n} = 0$
Adiabatic wall	$\boldsymbol{u}^-$ is given while other var. are taken as $\mathbf{U}^+ = \mathbf{U}^-$	$\mathbf{F}^{d,+}_{energy} \cdot \mathbf{n} = 0$, $\mathbf{F}^{d,+}_{mass} \cdot \mathbf{n} = 0$
Isothermal wall	$\boldsymbol{u}^-$ and T^- are given while other var. are taken as $\mathbf{U}^+ = \mathbf{U}^-$	$\mathbf{F}^{d,+}_{mass} \cdot \mathbf{n} = 0$
Subsonic outlet	P^- is given while other var. are taken as $\mathbf{U}^+ = \mathbf{U}^-$	$\mathbf{F}^{d,+} \cdot \mathbf{n} = 0$
Symmetry	$\mathbf{U}^+ = \mathbf{U}^-$	$\nabla \mathbf{U}^+ \cdot \mathbf{n} = 0$
Freestream	$\boldsymbol{u}^-, T^-, Y_i, P^-$ are given	$\mathbf{F}^{d,+} \cdot \mathbf{n} = 0$

Riemann solvers have been implemented. A Lax-Friedrich scheme is implemented and is appropriate for perfect gas. It can be extended to multi-species flow but is not well suited for low Mach number compressible flows, such as aerothermal flow encountered during reentry. AUSM$^+$*up* scheme is also implemented within Argo and allows to deal with low Mach compressible flows by splitting pressure terms and the convective terms.

A Simple Low dissipation AUSM (SLAU) Riemann solver was also implemented within Argo. It possesses similar behaviors than the AUSM$^+$*up* scheme and allows to treat multi-species flows. Regarding the application in aerothermal flows which are of interest here, this latter scheme will be selected throughout this work.

Diffusive variational terms

Diffusive terms in Eq. 3.7 are obtained using the Interior Penalty method (IP). IP methods were chosen for their compactness as only the direct neighbors are used to evaluate the residual and thus simplifies the evaluation of the Jacobian[14]. A Symmetric Interior Penalty (SIP) method for which $\theta = 1$ is used here and ensure a superior convergence. The penalty parameter α was derived by Shahbazi for the SIP method [44]. It is fixed to a value of 1.2 in this work, but should be investigated when diffusion coefficient is highly variable in space or either Non-Symmetric Interior Penalty (NSIP) method should be used to ensure the stability of the computation [41].

Boundary conditions

Within Argo, weak boundary conditions are implemented. For the convective part, ghost cell values are specified. A ghost cell is a virtual cell located on the other side of the inner boundary. For the hyperbolic Euler equations, those ghost cells values are in agreement with the number of characteristic entering or leaving the system. For the diffusive part, either Dirichlet, Neumann or Robin boundary conditions are implemented. Boundary conditions implemented within the *DGAblation* module of Argo are summarized in Tab. 3.1.

Time discretization

The problem of the ablation of a thermal protection material is obviously an unsteady phenomenon. Indeed, thermal degradation occurs inside the material, surrounding gas species react with the fibers and lead to the recession of the surface of the material. No steady-state is therefore expected to exist and unsteady numerical schemes must be considered, although Argo is featuring both steady and unsteady solvers. For the latter, explicit and implicit time stepping schemes are also possible. However, because of the strong reactive terms and sharp gradients at the interface of the porous medium, there are severe constraints on the time step for stability reasons and implicit schemes are foreseen.

Time implicit scheme

Considering again the vectorial system of equations (2.2) written as

$$\frac{\partial \mathbf{U}}{\partial t} = \mathcal{R}^{CDS}(\mathbf{U}), \tag{3.10}$$

where $\mathcal{R}^{CDS} = -\nabla \cdot \mathbb{F}^c + \nabla \cdot \mathbb{F}^d + \mathbf{S}$ and denotes the convective, diffusive and source terms. The time dependent problem is solved using a second order two-steps Backward Differential Formula (BDF2) and reads

$$\mathbf{U}^{n+1} = \mathbf{U}^n + \Delta t \mathcal{R}^{CDS}(\mathbf{U}^{n+1}) \tag{3.11a}$$

$$\mathbf{U}^{n+2} = \frac{4}{3}\mathbf{U}^{n+1} - \frac{1}{3}\mathbf{U}^n - \frac{2}{3}\Delta t \mathcal{R}^{CDS}(\mathbf{U}^{n+2}) \tag{3.11b}$$

This implicit scheme is a non-linear system that is solved using a Newton-Raphson (NR) algorithm. For the convergence of the algorithm, the Newton-Raphson needs an initial guess of the solution vector and the solution at the previous iteration is used. Therefore, when the solution is strongly affected by chemical reactions, or rapid change of properties between the flow and the porous region, the time step is also limited for the implicit scheme and must remain small. At each step, the estimation of the Jacobian is also required. In Argo, the Jacobian is implemented analytically but the differentiation can be done using a finite-difference approximation. The convergence is achieved using a relative criterion on the residuals or after a certain number of iterations is reached. Generally, a decrease of four order of magnitude is require on the residual.

The NR algorithm by nature requires also the resolution of a linear system at each iteration and the use of the Generalized Minimum Residual (GMRES) is chosen. The GMRES algorithm can be considered as an extension of the family of conjugate gradient methods for the resolution of linear systems. It was implemented by Hillewaert for DGM [14] and it features a matrix-free Newton-Krylov approach.

Computing the Jacobian increases with the number of DOFs and it can be computationally expensive. If the time step is sufficiently small, the computation of the Jacobian can be frozen during several iterations. Although the second order of convergence of the NR scheme is lost, this procedure allows to save calculation time. Most of the time this will be applied and the Jacobian is generally frozen between 3 and 5 iterations depending on the case.

Chapter 4

Simulation of Plasmatron Carbon Preform Experiments

This part mainly focuses on the numerical simulation of high-enthalpy experiments performed by means of the VKI Plasmatron facility. Reproduction of ablation experiments on carbron preform material are computed by means of the solver Argo (presented in the previous chapter). This is the first time that such reproduction of the complete experimental set-up of one ablation test is presented in literature.

In this chapter, a short introduction about the VKI Plasmatron facility is given in Sec. 4.1.1. Then the experimental set-up for the testing of materials and results of experiments are presented in Sec. 4.1.2. We will focus mainly on the single test case of a hemispherical shape carbon preform sample that was tested at high pressure and low heat flux. In Sec. 4.3, the corresponding numerical set-up for the same test case is then established and the boundary conditions are discussed. Finally, results from the numerical simulations are presented in Sec. 4.4. When possible, a comparison with experimental data is performed.

Experiments on material ablation

We introduce first in this section the *Plasmatron facility* where research experiments on both reusable and ablative materials have been tested for more than a decade now. In the second part, our attention will be mainly focus on experiments on ablative material tested inside the Plasmatron.

The VKI Plasmatron facility

The VKI Plasmatron is an Inductively Coupled Plasma (ICP) generator of high power (1.2 MW) which was inaugurated in 1997 and is still the most powerful facility of its kind in the world. Compared to arc-jet plasma wind tunnels[1], the ICP torch generates a more pure gas more suitable for GSI investigations.

The Plasmatron is based on an Inductively-Coupled Plasma (ICP) torch that preserves the heated plasma from pollutants, that were present within former combustion-heated facilities and arc-heaters. Combustion-heated facilities added heavy pollutants from combustion products while arc-heaters produced the electrodes to erode and both were not well-suited for TPS tests. Therefore, Plasmatron facilities using electrodeless technology

[1] An other type of plasma wind tunnel, that use electric arc discharge to heat up the flow.

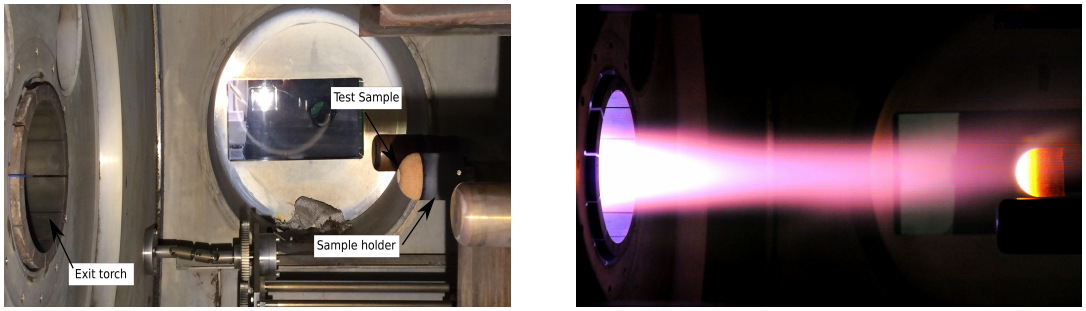

(a) (b)

Figure 4.1: Pictures of the experimental set-up of the Plasmatron. Left (a), photograph of the test chamber before basalt ablation experiment. Right (b), photograph of an ablation test of carbon-phenolic ablator AQ61 (1 MW/m^2, 15 hPA) by Helber [13].

for the plasma discharge ensure a superior flow purity and are usually more dedicated to the study of aerothermochemistry and gas-surface interaction phenomena.

At the exit of the torch, the subsonic plasma enters the test chamber, where the test sample is placed (Fig. 4.1). The chamber is usually kept at a pressure between 1200 and 25000 Pa, depending on the testing conditions. The plasma exists through a diffuser, and it is cooled down by a water-cooled heat exchanger. The vacuum system is based on a roots pump and a set of three rotating vanes pumps. After proper dilution, the products are finally released to the atmosphere through an exhaust. The overall facility is equipped with a cooling system using a closed loop deionized water circuit coupled to fan coolers.

Three parameters fully defined operating conditions of the Plasmatron during TPMs testing: the electric power supply P_{el} (kW), the pressure in the test chamber p_{tc} (Pa) and the mass flow rate of fluid $\dot{m}$ (g/s). These parameters are well-defined during a test and typical operating condition ranges are P_{el} between 120 and 300 [kW], p_{tc} between 1500 and 20000 [Pa] and the mass flow rate is often fixed to 16 [g/s][3].

The VKI Plasmatron was initially designed to test lifting body equiped with reusable TPS [4]. The recent work of Helber is the first investigation in the VKI Plasmatron on lightweight ablative TPMs [13]. Measurements of recession rate, shape change and gas-surface interaction phenomena were made and ablation limited to the surface was observed for the experiments on carbon preform (non-pyrolyzing carbon ablator). Measurements of pyrolysis blowing rate and mass loss were also performed on Asterm. The experimental test case investigated in this chapter is presented in the next section.

Plasmatron experiments on carbon preform

Several test cases on carbon preform samples were performed inside the Plasmatron. Different shapes (hemispherical, cylindrical), test gas (air, nitrogen) and test conditions (high and low pressure, high and low heat flux, subsonic and supersonic) has been investigated by Helber [13]. The experimental test conditions of the reference test case are given in Tab. 6.1.

This test case is made at 200 hPa and heat flux 1050 kW/m^2[2], that corresponds roughly to the re-entry condition of an orbital return. The hemispherical shape sample is chosen because it presents the most stable ablation condition with a fairly constant recession in the radial direction. This choice is also motivated by the relatively low heat flux transfer to the

[2]Compared to other test cases, this is a relatively high pressure and low heat flux

Test name	gas	p_s	P_{el}	$\dot{q}_{cw}$	τ	T_w	$\dot{s}$	$\dot{m}$	ϵ
		hPa	kW	kW/m^2	s	K	μm/s	mg/s	
HS-A2a	air	200	188	1050	91.2	1975	45 ± 1.4	53.2	0.86 ± 0.05

Table 4.1: Real Plasmatron test conditions for the reference test case (from Helber [13]). Hemispherical (HS) sample, test gas, static pressure p_s, generator power P_{el}, mean cold wall heat flux $\dot{q}_{cw}$, sample exposure time τ, mean surface temperature T_w, recession rate $\dot{s}$, mass loss rate $\dot{m}$ and emissivity of the surface ϵ.

material that results in lower mass loss, surface recession, wall heat flux and temperature jump between the flow and the material.

Test sample material

The material tested in this first simulation is a non-pyrolyzing Carbon-Bonded Carbon-Fiber (CBCF) material. The experimental material was provided by Mersen Scotland Holytown Ltd. (CALCARB®CBCF 18-2000 [33]) and the material response was investigated inside the Plasmatron [13]. The test material is a hemispherical sample of radius 25 mm, with total length of 50 mm (see Fig. 1.3a).

Centerline and volumetric recession

The volume loss of ablated samples was determined using High-Speed Camera (HSC). The camera is used to track the position of the interface of the sample. It appeared that hemispherical shape sample responds with a linear recession rate a few second after the plasma injection. Centerline recession rate obtained from measurement for test case of interest is given in Tab. 6.1. A total recession of $\backsim$ 4.45 mm was observed over the whole injection time.

Mass loss measurements

The mass loss can be estimated either by measuring the mass of the sample before and after the ablation experiments or using the volume loss obtained from HSC. In the second case, axisymetric ablation is assumed and the in-depth mass ablation is neglected. Mass loss rate obtained from weighting measurement is given in Tab. 6.1.

Discrepancies between the two method of measurements were observed ($\backsim$ 13% for the *HS-A2a* case) because of uncertainties on the density of the material (180 - 215 kg/m^3, that depends on the manufacturing), camera resolution, humidity and de-installation process from the sample holder.

Surface radiometry

Infrared radiometers provided information on the thermal behaviour of the material samples. Surface temperature is measured using a two-color pyrometer. They measure the radiance at two different wavelength ranges in order to get rid of the emissivity of the surface required in the gray body emission assumption. The emissivity of the test material was also determined using a broadband radiometer (only for the lowest surface temperature tests). An emissivity $\epsilon = 0.86$ (Tab. 6.1) was measured for the test case considered here. This material property is required for the numerical simulation as surface cooling due to radiation of the material surface is accounted.

Computation of the plasma freestream conditon

Most of the time a coupled numerical-experiment approach is used for the computation of plasma freestream conditions. First the subsonic freestream plasma flow coming from the ICP torch is characterized by a MagnetoHydroDynamics (MHD) solver. Then, the Boundary Layer (BL) edge condition obtained from the MHD solver are used as input for a boundary layer code. The code then rebuild the conditions at the BL edge of a non-reactive, catalitic BL by iterating on the outer edge temperature to wall heat-flux measurements. The freestream rebuilding procedure is briefly discussed below.

Freestream characterisation

A plasma is a gas that has the property to conduct an electric current when subjected to an electromagnetic field. Plasma jet generated by the Plasmatron facility belong to the field of the thermal plasma. Compared to other fields, like fusion plasma, thermal plasma are of relatively low temperature, and their temperature range is usually assumed to vary between 5000 and 25000 K. Inductive plasma generated inside the Plasmatron facility have a typical temperature about 10000 K at the exit of the torch.

A model for simulating such thermal plasma was developped by Magin [28] and plasma jet generated in the VKI Plasmatron can be numerically simulated using the VKI solver CooLFluiD[3]. The solver combines Navier-Stokes equations to the set of Maxwell relations for electromagnetism. For a numerical simulation, pressure in the test chamber p_{tc} and mass flow rate $\dot{m}$ need to be specified but also the electric power that is effectively transmitted to the flow. While the electric power supplying the Plasmatron facility is well-known as it comes from the network, the power transmitted to the plasma that is actually heating it is not well defined. It is only a fraction of the initial power supply and can be expressed as

$$P_{fl} = \eta P_{el} \ , \tag{4.1}$$

where P_{fl} is the electric power transmitted to the plasma flow and η an uncertain parameter. The effect of the uncertain parameter η on the freestream temperature and velocity profiles was investigated [7] and it was shown that this parameter was strongly influencing the temperature and velocity profiles. It was also shown this parameter is affecting the stability of the freestream plasma flow.

Boundary layer edge rebuilding

Once the plasma flowfield is characterized, it can be used as input to the boundary layer rebuilding solver. Therefore, conditions of the chemically-reacting boundary layer can be computed computed. The numerical simulations of the plasmatron experiments performed in this chapter are using as inlet conditions values coming from the BL rebuilding. A constant temperature and velocity profile over the whole inlet are then assumed.

Numerical simulation of ablation experiments

Experiments and measurement of an ablation case has just been presented. The numerical test case is now presented with the hypotheses made. The computational domain and boundary conditions are first introduced. Then, modelling of the solid and the fluid phase, as well as the gas-surface reactions are presented.

[3]Computational Object-Oriented Libraries for Fluid Dynamics.

Computational domain and boundary conditions

Compared to the Plasmatron experiment, not all the domain represented in Figs. 4.1 is considered. The inlet boundary is 13 cm away from the sample surface. The length of the holder behind the material is 25 mm. The whole computational domain is shown in Fig. 4.2 with the corresponding boundary conditions. It worth to emphasize that there is no boundaries between the fluid medium and the solid material. Only a refinement in the mesh is performed close to the surface in order to catch the recession of the surface. This refinement is also necessary regarding the physics, because this part of the domain is subjected to high variations (for example, the temperature varies from 6000 K in the freestream to 298 K inside the material).

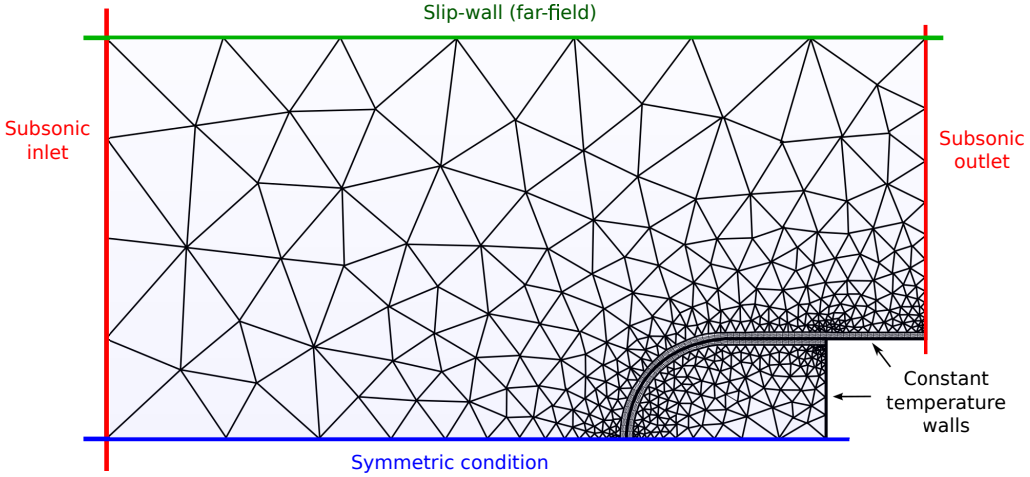

Figure 4.2: Computational domain of the Plasmatron experiment.

The unstructured mesh is composed of 2256 triangular elements. The total number of elements is relatively low, but the number of degrees of freedoom becomes relatively high when considering several mixture species. A first order Lagrangian polynomial interpolation is used on each elements. Tab. 4.2 summarizes the computational performance of the numerical experiment.

Table 4.2: Summary of the computational performances and characteristics of Plasmatron carbon preform simulations.

Test Case	Nb of time step	Nb of elemts	Nb of DOF	Nb of CPUs	CPU time
HS-A2a coarse mesh	198000	1457	$1457 \times 3 \times 10$	12	≈ 3 weeks

A special care is needed with regard to the cells close to the surface and a few comments are made in the next paragraph.

Boundary layer refinement

We would like to emphasize the importance of refining the mesh close to the surface of the material. There are two reason for this refinement:

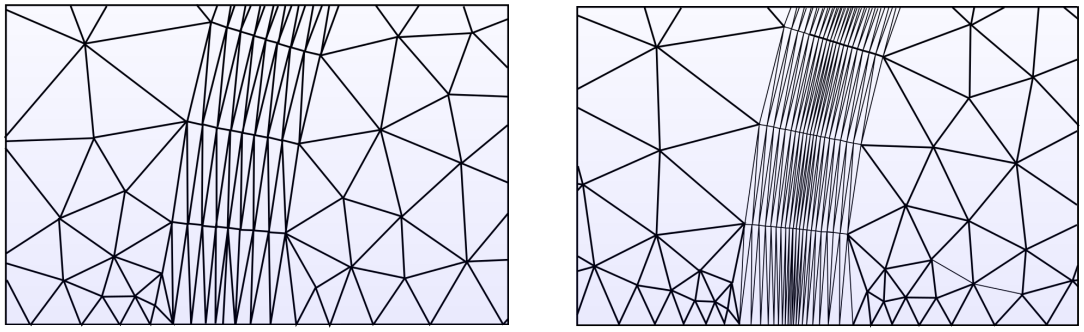

(a) Coarse mesh (b) Fine mesh

Figure 4.3: Mesh refinement close to the boundary layer of the porous material. Example of a coarse mesh (a) and a fine mesh (b).

Table 4.3: Summary of the boundary conditions for the Plasmatron test case. The species mass fractions are express in the following order: $\mathrm{N}, \mathrm{O}, \mathrm{NO}, \mathrm{N_2}, \mathrm{O_2}, \mathrm{CO}$.

Subsonic inlet	$U_{in} = 37$ ms^{-1}, $T_{in} = 6088$ K $Y_{in} = \{0.27, 0.23, 0.0036, 0.49, 5e\text{-}5, 0\}$
Subsonic outlet	$p_{out} = 20000$ Pa
Constant temperature wall	$T_w = 298$ K

- First of all, strong gradients are expected close to the surface of the material (temperature, velocity) as well as strong chemical production of species from homogeneous and heterogeneous reactions.

- Secondly, recession of the material need to be tracked.

In Fig. 4.3, an example of a coarse mesh and a fine mesh at the interface are presented. These two configurations were both tested for the same test case of Plasmatron experiment. Because of the relatively poor refinement of the coarse mesh Fig. 4.3a, an increase in the solid mass and no recession were observed in the material, although other quantities such as the temperature increase at the surface were correctly caught. The second mesh on the right is a mesh that allowed to catch the recession. The finest cells in Fig. 4.3b are 43 μm in the axial direction while they are only 200 μm for the coarse mesh.

Boundary conditions

Boundary conditions are now adressed. The case of the inlet condition was already mentioned previously. The rebuilding of the freestream flow is extracted using the VKI 1-D boundary layer code [49]. The freestream value obtained from the 1D simulation is imposed on the whole subsonic inlet. Species mass fraction at the inlet are obtained from the equilibrium composition of a mixture air with 5 species. The pressure at the outlet is the one corresponding to the experimental set-up (Tab. 6.1) and is equal to 200 hPa. Boundary conditions are summarized in Tab. 4.3.

Solid phase

The material tested in this first simulation is the non-pyrolyzing Carbon-Bonded Carbon-Fiber (CBCF) material already presented in Sec. 4.1.2. The following assumptions are made for the numerical simulation

- Fibers are made of carbon. No preferential direction in the fibers are modelled, that would results in non-scalar material properties. The initial radius of the fibers is equal to
- The material has a bulk nominal initial density of 180 kg/m^3 with an initial porosity of 90%.
- Thermal conductivity is provided by the manufacturer and a constant value of 0.5 W/m-K is used.

Permeability and tortuosity

In addition, permeability and tortuosity must be provided to the code for the closure of the system of equations. Contrary to the properties mentioned previously, these two are not given by the manufacturer and can not be obtained by experimental measurements. For the permeability, an initial value of 1.45e-10 is chosen and it is assumed to evolve with porosity according to the semi-empirical model of Carman-Kozeny (2.18). Concerning the porosity, an initial value of 1.1 is adopted and it evolves linearly between freestream tortuosity ($\eta = 1$) and its initial value (see Eq. 2.16).

Fluid phase

The fluid is made of N_s chemical species, each considered as a thermally perfect gas. The fluid is considered to be a mixture of 6 species: 5 for the inflow air (N_2, O_2, N, O, NO) and one product of oxidation (CO). Finite rate chemistry for the homogeneous are used. Products of reaction CO are assumed to be frozen and they do not react with the surrounding gas. Transport coefficients are computed with the Chapman-Enskog method. Thermodynamic properties are computed by means of statistical mechanics, considering rigid rotator and harmonic oscillator model for the molecular species rotation and vibration. Diffusion fluxes are computed by means Fick law complemented with a Ramshaw correction.

Thermodynamic and transport properties, diffusion coefficients as well as the finite rate coefficient for the homogenous reactions are obtained using collisional data from Mutation++ library, already introduced in Chap. 2.

Surface reaction rates

Chemical reactions between the fluid and the solid need to be modelled. There are really important as they are mainly responsible of the surface ablation of the material. In this case, only chemical reactions induce the recession of the surface (no sublimation and no mechanical erosion). The following surface reactions are considered within this work

$$\mathrm{O} + \mathrm{C}(s) \rightarrow \mathrm{CO} \tag{4.2}$$

$$\mathrm{O_2} + 2\mathrm{C}(s) \rightarrow 2\mathrm{CO} \tag{4.3}$$

for which reverse reactions need not to be considered as the equilibrium constant is very small[39]. The presence of CN was also observed experimentally by means of Optical

	Reacting species	
	O	O_2
A	3.22	5.73
E_a	0	$9.65e3$
n	0.5	0.5

Table 4.4: Arrhenius coefficient for oxidations reactions of carbon fibers.

Emission Spectroscopy (OES) [13] but reactions with atomic nitrogen are however not considered here. The forward reactions rates for the two previous reactions are obtained from Arrhenius type law of the form

$$k_f^{i,\mathrm{C}(s)} = AT^n \exp\left(\frac{-E_a}{T}\right) \tag{4.4}$$

where i denotes the limiting species. The Arrhenius coefficient are given in Tab. 4.4 [39].

For the heterogeneous reactions (2.23), a model for the recession of the fibers needs also to be defined for the computation of the specific surface. In this case, it is assumed that the fibers are cylindric-shaped and that they recess uniformly in the radial direction. In also worth to note that no wall catalicity is considered at the surface of the material.

Results

Results of the numerical simulations are now presented. The physical time during which the simulation takes place is equal to 20 s. This is much lower than the real injection time inside the Plasmatron, but it is enough to reach the quasi-steady state for recession observed on hemispherical-shape samples. An other reason of that lower simulation time is the computational cost. Some words about the freestream flow at the initialisation is first given.

Analysis of the freestream transient behaviour

The flow is characterized by different time scale in the overall domain. When lauching a plasmatron test case, one need first to obtain a semi-steady solution. By semi-steady, we mean a solution were the freestream flow is globally in a steady-state, although heat conduction, convection and ablation (chemical reactions) may occur inside the material. Therefore, to initialise the flow, the time step is progressively increased and helps to resolve the different phenomena that occur at different time scales. This multi-step methodology avoids to have physical phenomena that are too sharp inside the whole domain and help the solver to converge. Generally the time required for the flow to reach the semi-steady state is of the order of $5e-05$ s (domain length of 2 cm, fluid velocity 37 m/s). During this time, the reactions that would occur at the surface of the material will be negligible on the overall recession/chemical reactions during the total injection time (90 s). The initial time step is limited by pressure waves that propagates at the beginning of the simulation. Those ones travel at the speed of sound and therefore a time step lower than $1e$-5 must be used.

Reflective boundary condition

When pressure waves first reached the outlet pressure condition, they are reflected and come back toward the inlet that are reflected again. These back and forth reflections can strongly affect the convergence at the beginning of the simulation. There are different strategies to avoid the propagation of the pressures waves inside the domain.

- Using non-reflective boundary conditions at the inlet and the outlet. No non-reflective boundary conditions are implemented in the DGAblation module and unwanted waves reflection will be present in the domain as pressure is imposed at the outlet[4]. As suggested already by Schrooyen, Navier-Stokes Characterstic Boundary conditions (NSCBC) or Perfectly Matched Layer (PML), could be implemented [42]. They are neither investigated in this work but it can be sought as a future work.

- Initialising the flow with a constant, but non-physical, species partial pressure and assuming that no homogeneous chemical reactions occur. By doing this, one can avoid to have the propagation of the wave due to species partial pressure when imposing a high-temperature inlet where the species are dissociated.

- Using a coarse mesh at the inlet and the outlet. The pressure waves will propagate inside the whole domain back and forth on the inlet and the outlet until they are damped by the coarse mesh. The size of the cells required to damp those waves is not easy to determine and the coarse mesh is roughly determined by means of trial and error tests. This is in contrast with the necessity of having a fine mesh at the interface and renders the creation of such mesh quite difficult. However, the analysis of the transient behaviour will be closer to the real physical behaviour.

The two latter strategies have been investigated in this work and they were shown to provide the same results for the established flow. In the last approach, the time step must be fine enough to catch the pressure waves that propagates at the speed of sound inside the domain. The second methodology was used because waves propagation wave not the interest in this work.

Surface temperature

Once the freestream flowfield reaches the material, this one will start to be heated. Because of the low density and relatively low thermal conductivity of the material, compared to pure graphite, a very fast increase in the temperature can be observe. Gas-surface interaction is also responsible of this fast increase. The lower temperature of the material compared to the freestream temperature generates recombination of atomic species close to the wall and in particular because of atomic nitrogen (see later Fig. 4.6). Those recombination reactions are exothermic, as well as for the oxidation reactions with the fibers.

Compare to experimental results, it can be noticed that the rate of temperature rise is slightly slower for the numerical results. This can be explained by the constant thermal conductivity of 0.5 that was used for this first test. Thermal conductivity indeed change with temperature and according to the manufacturer, the value is lower than 0.5 at low temperature. So at the beginning, the material tested numerically is less isolating than the real one.

[4]Note that pressure waves could also be present in real Plasmatron test as the experiment takes place inside a closed chamber. The reflection observed here are however purely numerical.

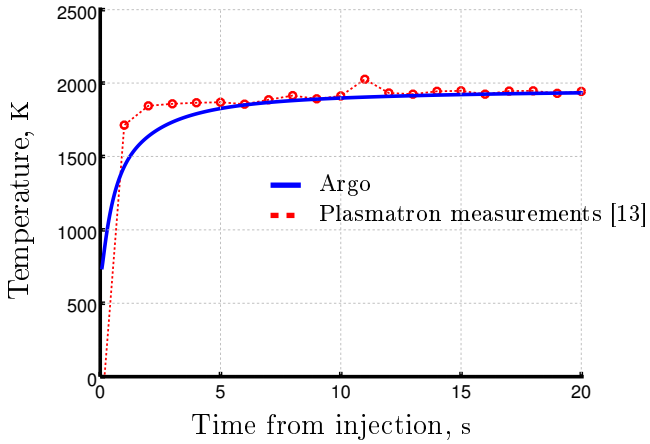

Figure 4.4: Surface temperature of the carbon preform material inside the Plasmatron.

The correspondence between the two maximum temperature was obtained by defining the surface of the material at 70% of its maximum density value. The heat capacity of the material being uncertain, the maximum value of temperature can change.

Static pressure

Static pressure

The result for the static pressure along the stagnation line is shown in Fig. 4.5 and is extracted after the initialisation of the freestream flow (0.2 s). A peak at 20009 Pa is observed at the surface of the sample. A simple estimation of the pressure at the wall can be obtained using Bernouilli's principle on the stagnation line

$$p_w = p_s + \frac{\rho u^2}{2} \tag{4.5}$$

where ρ and u and the freestream density and velocity. The density of the gas at 6088 K is 0.007677 kg/m^3 and the velocit being equal to 37 m/s, a value of 20005 Pa is obtained. This simple estimation does not consider compressible effects but are negligible at low Mach number. However, a correction for viscous effect that arises at low Reynolds number (Barker effect), typically below 100, can be used for the estimation of the stagnation pressure

$$p_w = \frac{1}{2}\rho u^2 K_H + p_s \tag{4.6}$$

where K_H is the Homann's correction factor [15] given by

$$K_H = 1 + \frac{6}{Re + 0.455\sqrt{Re}}. \tag{4.7}$$

The Reynolds number is based on the radius of the sample and the freestream conditions, leading to $Re = 42.3$. Bernouilli's formula with the Homann's correction gives a static pressure at the wall of 20006 Pa. Both approximation give results closed because of the relatively large radius of the sample, compared to small pitot probes on which the effect can lead to error larger than 10% [30]. The two approximation are close to the numerical result with less than 0.1% of difference.

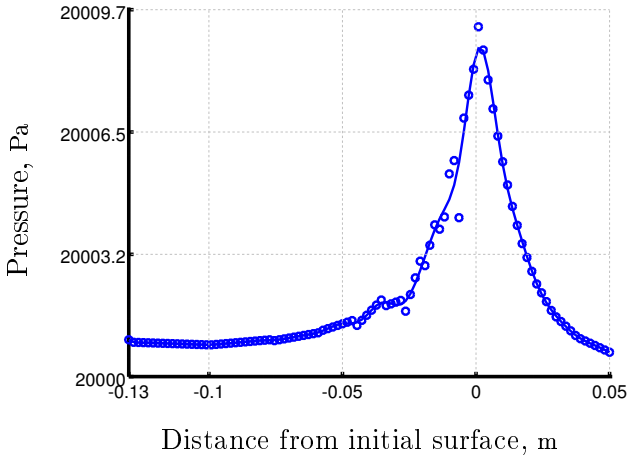

Figure 4.5: Stagnation line static pressure. Circles are the raw data and the continuous line is the smoothed curve.

Species partial pressures

One of the main advantages of the code is that one mass equation per species is solved at each time step. This allows to track the production of species from heterogeneous chemical reactions and also the different partial pressures inside the whole domain. The results obtained from each partial pressures at two different time are showed in Fig. 4.6.

In Fig. 4.6a, partial pressure are shown at the beginning of the simulation (0.2 s) is shown. A peak of CO is observed at the surface that arises from the reaction of carbon with the oxygen species (both O_2 and O). The production at the surface comes mainly from the reaction with atomic oxygen, that is also diffusing inside the material on a distance l_{abl} also called the ablation depth. The production of CO inside the domain comes from diatomic oxygen that is present initially inside the material. O_2 species are consumed and partial pressure goes to zero.

In Fig. 4.6b, the CO has diffused inside the material and the partial pressure is barely constant. The production of CO then reaches a steady state at the surface.

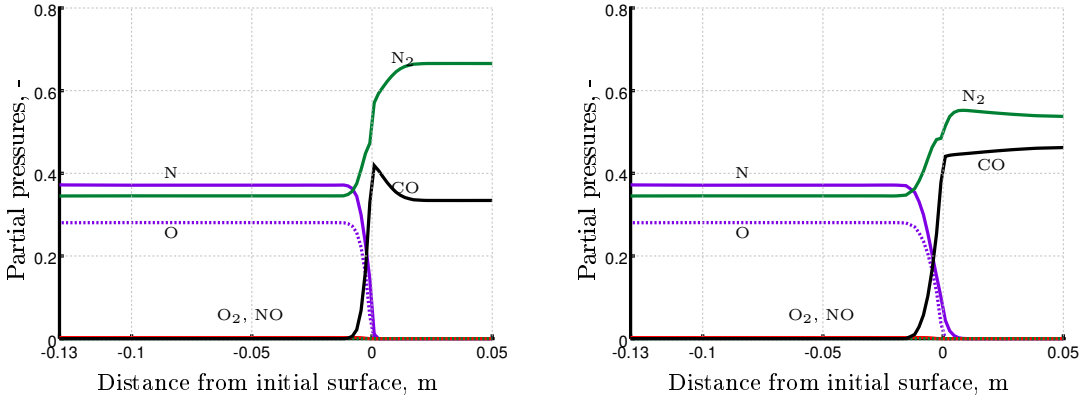

(a) $t = 0.2$ s (b) $t = 20$ s

Figure 4.6: Species partial pressure along stagnation line.

Length of ablation

It was stressed in Chap. 1 that previous numerical codes were assuming ablation as a surface phenomenon only. This assumption was widely used in the past for the design of heat shields using dense TPMs, but the use of low-density material with high porosity requires the modification of this hypothesis. The ablation phenomenon for lightweight materials was shown to occur also below the surface of the sample [38]. The Thiele number reflects the competition between surface and volume ablation

$$Th = \frac{L}{\sqrt{D_{eff}/S_f k_f}} = \frac{L}{l_{abl}},$$

where l_{abl} is the length of ablation driven by oxygen diffusion and fiber reactivity. The oxygen penetration depth l_{abl} can be directly obtained from the numerical simulation, observing the depth at which atomic oxygen decreases towards zero. The position of the surface is tracked using the same definition as previously and the ablation length is found to be equal to 79 μm. The correspond Thiele number is $Th = 316.41$. For the comparison, the length of ablation was found to be 66 μm and $Th = 360$ experimentally for the same test case. Value of a $Th > 50$ suggests a diffusion-limited ablation process[5]. Discrepancies may be explained by the difference in the radius of the fibers used, modifying the specific surface, on the accuracy of the mesh, for which smallest cells are close to the length of ablation, and the definition of the surface, for which we used the position at which density is at 70% of its maximum value.

Solid density and mass

Solid density recession and total mass decreased was obtained on the fine mesh. The coarser mesh didn't allow to catch the recession of the surface, although the other quantities were well defined. A refinement at the interface was therefore performed but no long run simulation for solid mass and surface recession is available. The results obtained on 1.7 s of simulation are shown in Fig. 4.7.

Velocity fields

Axial velocity and gradient of the velocity are computed along the stagnation line. Axial velocity (Fig. 4.8a) starts to decrease noticeably at 5 cm upstream the sample and goes to zero. The bumps in the axial velocity profile are due to the coarse cells away from the sample surface. Close to the surface, a negative value of velocity is observed and will be explained in the next paragraph. Velocity gradient is shown in Fig. 4.8b. Velocity gradient is one parameter required for the rebuilding of real flight condition [50]. Because of the first order approximation of the elements, velocity gradient is piecewise constant. The continuous curve represent the fitted data. Boundary layer edge is generally estimated using the inflection point of the velocity gradient in the increasing part of the curve. Because of the bad approximation, inflection point cannot be located accurately, but can be estimated to lie close to 25 mm in front of the sample. It can be notice also that the velocity gradient does not decrease directly to zero value at the sample surface because of the flow field inside the porous medium.

[5]Thiele number for NASA flow tube experiments [38] were closed to a value of 2, in which volume ablation was observed

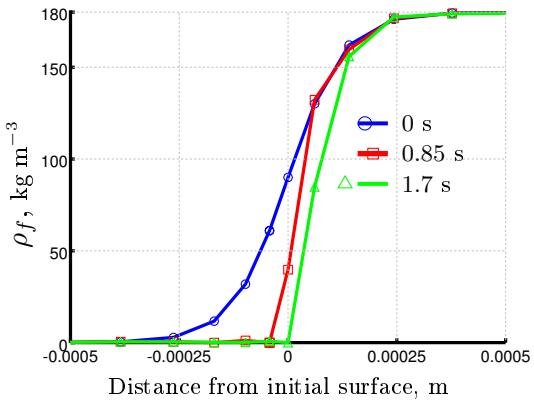

(a) Average solid density

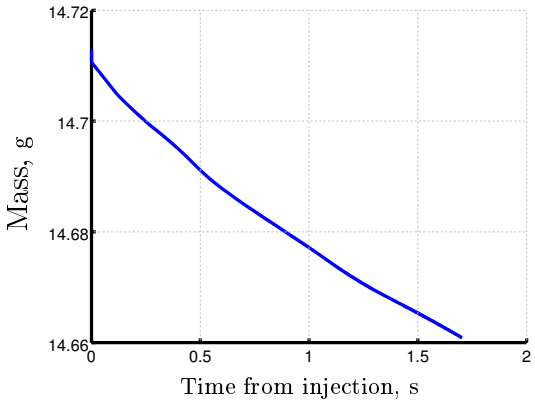

(b) Solid mass

Figure 4.7: Variation of the solid density close to the surface along the stagnation line (a) and total mass variation of the carbon preform sample as a function of time (b).

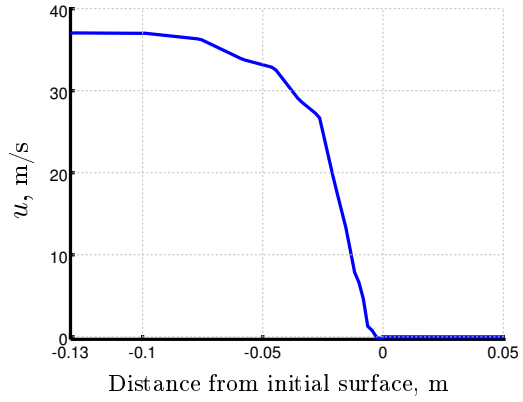

(a) Axial velocity

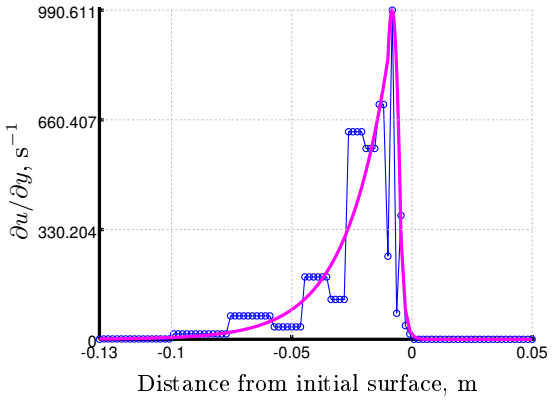

(b) Velocity gradient

Figure 4.8: Axial velocity (a) and velocity gradient (b) along the stagnation line at $t = 20$ s. First order approximation on the elements gives a piecewise constant velocity gradient function (b). Continuous line is the smoothed data.

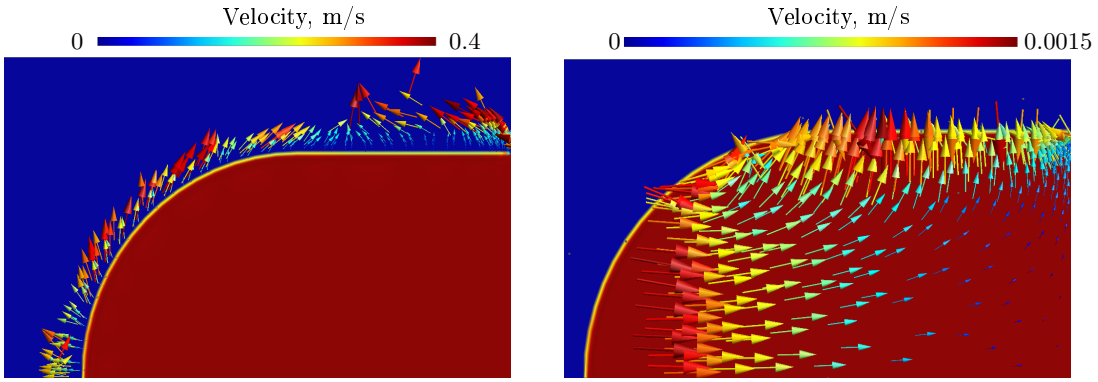

(a) (b)

Figure 4.9: Velocity vector field at the edge of the material (a) and inside the porous medium (b).

Velocity field inside the porous medium

Close to the outer part of the surface, a backward flow can be observed due to the heterogeneous production of carbon monoxide that releases gas in the boundary layer. Inside the porous material, a flow of low velocity (Stokes flow) is observed, ranging from 0 to 0.01 m/s on the edges of the material. The velocity vector field inside the porous medium is shown in Fig. 4.9. Note that at the shoulder of the sample, a backward flow can be observed and is due to the influence of the outlet. Ideally in order to reduce the influence of the outlet, this one should be kept away.

Review of the chapter

A complete reproduction of one Plasmatron experiment, corresponding to a high pressure and low heat flux test, was performed in this chapter.

The solution was computed using first order elements. For a better accuracy of the solution, the order of the elements should be increased. This would allow for example to have better estimation of quantities such as the gradient velocity that was presented before and therefore have an estimation of the BL edge. This would also help the solve to converge better close to the gas-solid interface. However, the overall computational time increases with the approximation order.

Two different types of mesh were tested with two different refinement at the interface of the solid. It was observed that the cell size needed to be fine enough in order to catch the phenomenon related to ablation. An estimation of the length of ablation may be used to define the order of the finest cell at the interface. As already stated, increaseing the order of the polynomial approximation may allows to increase the accuracy at the interface while using the same cell size.

Chapter 5

Verification Test Cases for the Pyrolysis Module

The pyrolysis module that was implemented in Argo was described in Chap. 2. The next step is then to verify that the code is producing correct results. A first simple test case is used to verify the implementation on a pure heat conduction, then pyrolysis reactions are added to the problem. The simple 1D code Echion, developed by Schrooyen [42] is used as a code-to-code comparison. This code was developed to demonstrate the capability of a discontinuous Galerkin approach to simulate flow in porous media. It was furthermore validated on PATO [25]. These two numerical solver (Echion and PATO) are both material response solvers (see Sec. 1.2.2) and therefore do not integrate a fluid part in the computational domain. Same laws of conservation for the thermal degradation of a resin content and of conservation of energy are implemented. However, the momentum conservation law (1D) is described by a simplified Darcy's law.

Therefore, in this chapter, only test cases with single porous material and no outer fluid phase are considered. In Sec. 5.1, the thermal properties for the ablative composite material used in this chapter are presented. Then in Sec. 5.2, the numerical set-up of the verification test case is presented as well as the boundary conditions. The implementation is verified for two physical phenomenon: a pure conduction on an ablative composite material in order to test the implementation of the thermal properties (Sec. 5.3) and a pyrolyzing test case which considers only thermal degradation (no charred recession) (Sec. 5.4).

Thermodynamic and transport properties for pyrolyzing material

The thermodynamic and transport properties for the virgin and the charred matrix are taken from the Theoretical Ablative Composite for Open Testing (TACOT). The property values themselves are obtained from PICA thermal response experiments, for which the properties were derived by a process of matching FIAT model predictions to experimental arc jet data [8]. The TACOT properties are available in the open literature and is therefore well suited for material response code comparisons [21], [22].

Thermal conductivity

Thermal conductivity of the TACOT is an average between the fluid and the solid phase. Therefore, the effective conductivity implemented in Argo in Eq. 2.21 must be changed

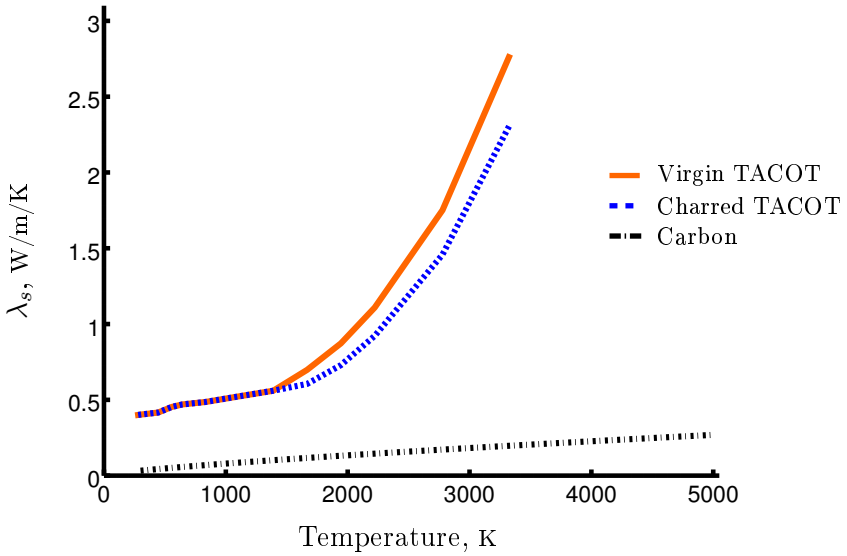

Figure 5.1: Comparison of the solid thermal conductivities of the virgin TACOT, charred TACOT and solid carbon.

when considering the TACOT material in order not to take two time the gas conductivity in account.

The material conductivity is assumed to change linearly with the global advancement of the pyrolysis process ξ between virgin and charred solid conductivities as

$$\lambda_{eff} = (1 - \xi)\lambda_s^v + \xi\lambda_s^c \tag{5.1}$$

Thermal conductivity is a function of temperature and is fitted using a $4th$ order polynomial. The theoretical validity temperature range is $T < 3333K$, but these values are extrapolated for higher range when required. When all pyrolysis reactions are completed, the solid conductivity remains constant. The virgin and charred conductivities are plotted in Fig. 5.1. For the comparison, the thermal conductivity of pure carbon is also represented.

Permeability and tortuosity

Initial permeability and tortuosity were also derived for the TACOT material. Permeability is expressed here using the linear model from Eq. 2.19.

Enthalpy and heat capacity

The TACOT properties are fitted to the NASA-7 polynomials for they used in the internal library of Argo. They are shown in Fig. 5.2 for the virgin and char states.

Ablation Workshop Test Case 1

A series of test case have been imagined recently for comparing the different codes for ablative-material simulation [21], [22]. These test cases are generally used to validate new solvers and to observe the effect of the different hypotheses on the model implemented.

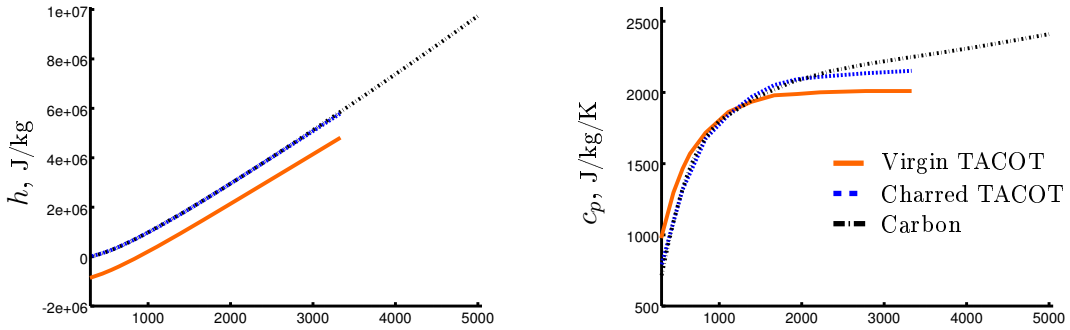

(a) Solid enthalpy

(b) Solid specific heat

Figure 5.2: Enthalpy (a) and specific heat (b) of the solid material and comparison with pure carbon.

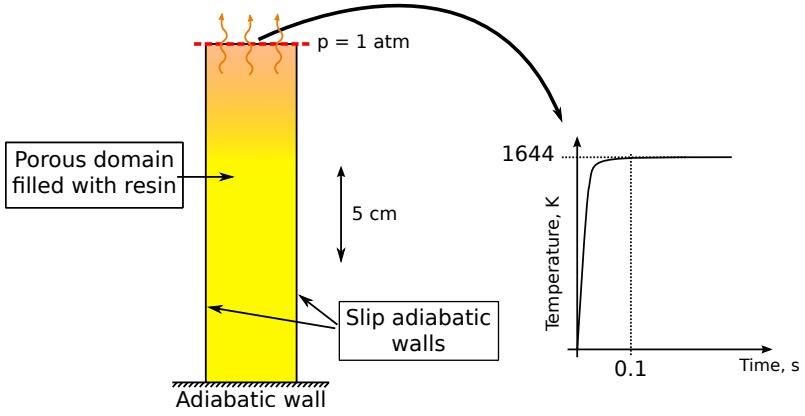

Figure 5.3: Sketch of the domain and boundary conditions for the Ablation Workshop test case.

The first ablation test case is a simple geometry in which no recession is considered. In this case, we consider two cases, one where no reaction pyrolysis occur during the heating and an other one where chemical reactions occurs. The first case will allow to verify the pure conduction inside the material. All the hypotheses are the same comparing Argo and Echion and the results should be very similar. The second test case, results are expected to change slighly.

The mixture for the test case is a simple one composed of only CO species. By doing this, the problem of diffusion through the surface of the material that can lead to numerical difficulties is suppressed. The simple mixture of CO has moreover thermodynamic properties of the same order as for the real pyrolysis gases. A sketch of the computational domain is given in Fig. 5.3. The material sample is heated from the top during 60 s at a temperature of 1644 K. The temperature increases gradually during 0.1 s before reaching its maximum value. The domain is 5 cm high and is composed of carbon fibers with phenolic-resin matrix. Thermodynamic and transport properties of the resin are taken for the fake TACOT material, which is used for the comparison with other codes. In this simple case, no need to specify mass fraction as the number of species is equal to one. The mesh is composed of 160 quadrilateral elements with a refinement close to the surface.

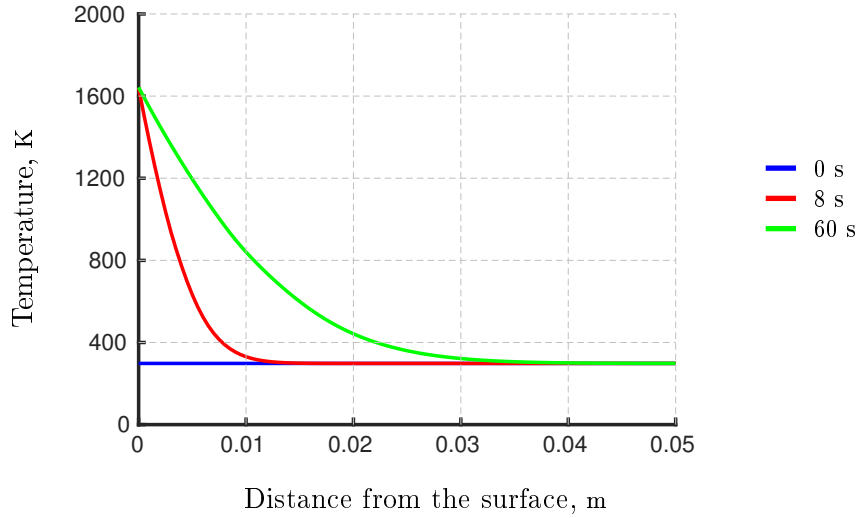

Figure 5.4: Surface temperature of the test sample.

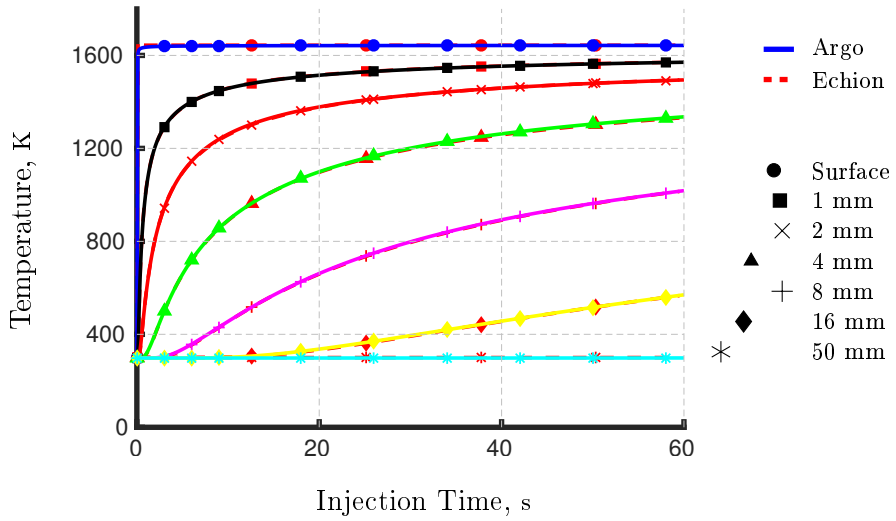

Figure 5.5: Temperature inside the material (thermocouples).

Pure conduction

A first simulation of pure heat conduction in the material is first tested by deactivating the pyrolysis reactions. The same results should be obtain between Argo and Echion as the heat equation is the same for both. The material is heated during 60 s from the top surface. Temperature propagates inside the material towards the end of the domain as shown in Fig. 5.4. The total length of the material is long enough in order that the bottom boundary does not influence the conduction inside the material.

For the comparison, the temperature is extracted at different position below the surface of the material and the evolution of these "thermocouples" are computed as a function of the injection time. Results are shown in Fig. 5.5.

As expected, the temperature extracted at the different thermocouples show a very good agreement with the material code Echion. Indeed, a difference of less than 1% is observed between the two codes.

	Resin A	Resin B
A_0	1.4e4	4.48e9
$E_a/\mathcal{R}$	85556.53	20441.26
n	3	3

Table 5.1: Arrhenius coefficients for the thermal degradation reactions [12].

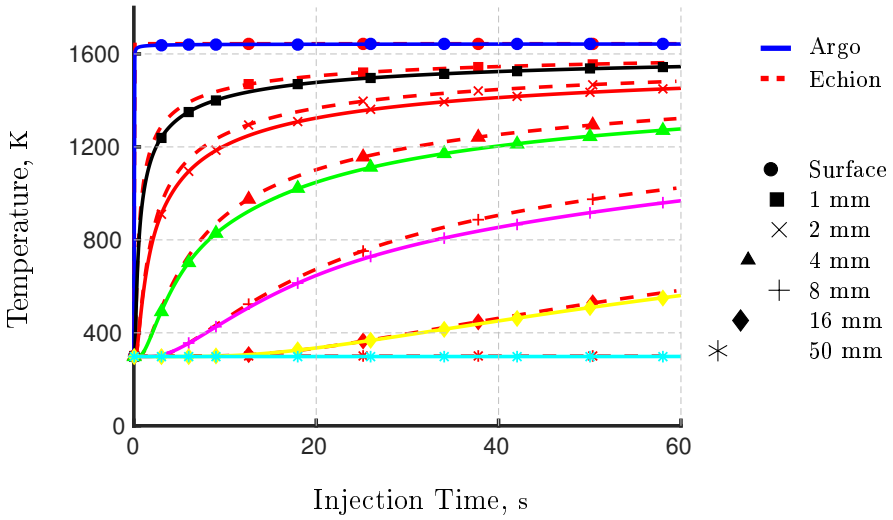

Figure 5.6: Temperature inside the material (thermocouples).

Pyrolyzing material with no surface recession

For the second test case, the thermal degradation of the resin in considered. There is no recession of the fibers and the surface position remains constant. Therefore, the material is losing mass only due to the pyrolysis of the resin. The thermal degradation rate are coming from Goldstein thermogravimetry analyses [12] which are fitted to Arrhenius type law, recalled here for[1] convenience

$$\frac{\partial \rho_{m,I}}{\partial_t} = -A_{0,I}\rho_m^v \exp\left(\frac{-Ea_I T}{\mathcal{R}}\right)\left(\frac{\rho_{m,I}^v - \rho_{m,I}^c}{\rho_{m,I}^v}\right)^{n_I} \tag{5.2}$$

The resin is decomposing at two different rates according to the model of Goldstein [12]. The values for the Arrhenius coefficients are summarized in Tab. 5.1.

Once again, the results of the thermocouples are plotted against the results obtained from Echion and are showed in Fig. 5.6. Results show to be in good agreement at low temperature, when the material starts to heat up at a given location. When the temperature rises above roughly 500 K, the curves starts to diverge slightly and the temperature computed with Argo reaches a lower value. This difference is attributed to the different law for momentum conservation that is implemented in the two codes.

[1] Average brackets are omitted for simplicity but variables are averaged quantities

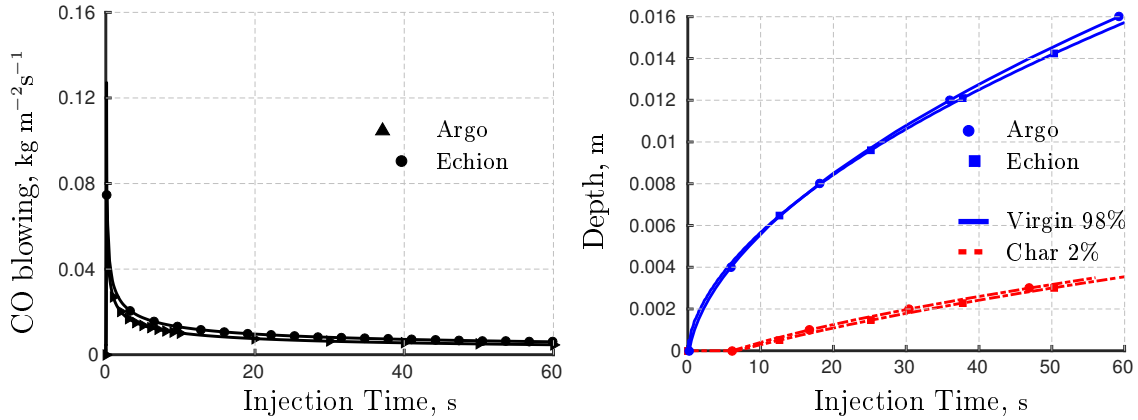

(a) Pyrolysis gas blowing.

(b) 98% virgin and 2% char fronts.

Figure 5.7: Comparison of CO blowing, virgin and char edges obtained with Echion and Argo solvers.

Mass blowing, char and virgin zones

For the pyrolyzing material, mass blowing through the top surface can be computed and compared as well with other material codes. The blowing through the surface is given by the density of the gas times the velocity through the surface. The single mixture species considered here was the CO and the blowing rate is shown in Fig. 5.7a. Results are again plotted against Echion. A lower value for the blowing is observed with Argo but the two results are in close agreement. This was expected as the temperature obtained with Argo is lower and so is the rate of decomposition of the material.

The position of the virgin and the char zones within the material are also compared. The front of the zone is defined using a thresholds value for the resin and charred densities given by

$$\rho_t^v = \rho_m^c + 0.98\,(\rho_m^v - \rho_m^c)\,, \tag{5.3}$$

$$\rho_t^c = \rho_m^c + 0.02\,(\rho_m^v - \rho_m^c) \tag{5.4}$$

where t stands for *threshold* value. Results are shown in Fig. 5.7b and shown to be again in good agreements with Echion. Discrepancies of less than 5% are observed.

Review of the chapter

A module accounting for the pyrolysis and the charred decomposition of a ablative composite fiber-resin materials has been added to the Argo solver. The new module was validated on two simple 1D test cases, one accounting for pure conduction and the other accounting for pyrolysis of a phenolic resin. Thermodynamic and transport properties of the TACOT material were used and good agreements with the numerical solver Echion were observed. The test case accounting for pyrolysis shown slight differences with the material code and they were accounted to be due to the different momentum conservation law implemented in the two codes. Finally, it was not possible to validate a full test case accounting for pyrolysis and charred recession because of the lack of material properties and available and numerical test cases in literature for code-to-code comparison.

Chapter 6

Simulation of Pyrolysis Experiments

One of the issue associated with the numerical testing of ablative material is the lack of data available in literature. Most of the time these materials are under restrictions. Many effort have been provided to the development of a database for the scientific community, as the TACOT material presented in the previous section. However this fake material is not suitable for all numerical approaches; for the unified approach investigated in this work, data on the solid material itself are needed for the evaluation of the thermodynamic and transport properties. Such data already exists for the Calcarb [33] that were used for the simulations of carbon preform experiments. However, those data are generally limited and for more sophisticated material they don't even exist. Some attend to develop material properties for the scientific community is currenly under development, as it is the intend of the ZURAM R material developed by the DLR [52] in order to provide material properties for the validation of numerical codes, as well as developing a database for code-to-code comparison. Properties coming from experimental measurements will provide data for future numerical simulations.

In this chapter, a first attempt to simulate Plasmatron experiments on pyrolysing material is performed. For that, a new set of properties is first proposed for the unified approach and presented in Sec. 6.1. Then the numerical set-up is briefly reviewed and finally the first results a presented and discussed.

Material properties

As introduced in the introduction of this chapter, properties that are valid inside the fluid and the solid are required when considering the unified approach. Considering again the effective thermal conductivity in Eq. 2.21 it can be seen that the properties for the intrinsic solid phase as well as for the gaseous phase are required when the average is performing. Therefore, due to the lack of open data literature, a trick is used in this work to define properties for the material itself. Virgin and the char thermal conductivites from TACOT material are used, from which is substracted the thermal conductivity of air (simplified mixture of air with 5 elements computed with Mutation++). By doing this, the properties of TACOT are retrieved inside the porous medium for the initial virgin and charred state while in the fluid only properties of air are considered. Between the virgin state and the charred state, the properties decrease with porosity (again with the pyrolysis advancement coefficient).

A similar approach is used for the internal energy (enthlapy) and specific heat of the solid material. In this case, the new properties intrinsic to the matrix phase are obtained

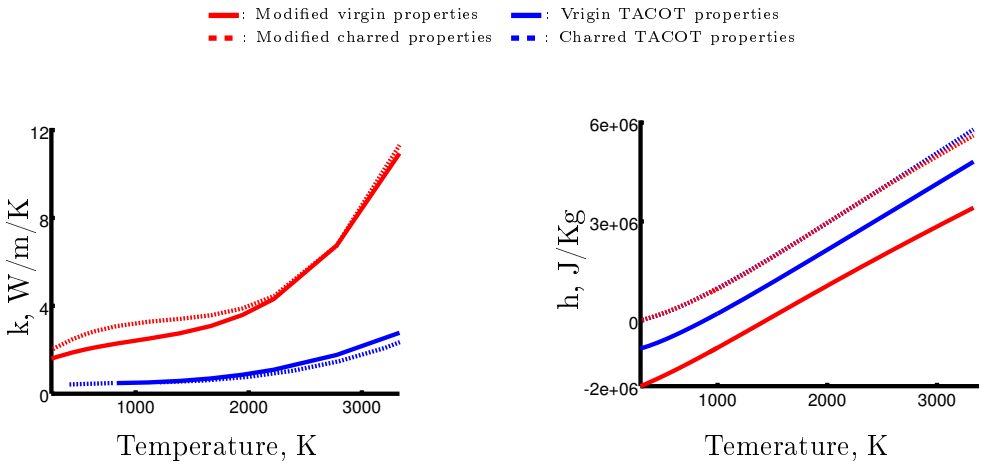

(a) Thermal conductivity

(b) Enthalpy

Figure 6.1: Modified material properties that are used for the unified approach.

by considering that

$$\langle \rho_f \rangle \langle e_f \rangle + \langle \rho_m \rangle \langle e_m \rangle = \langle \rho_s \rangle \langle e_s \rangle, \tag{6.1}$$

$$\langle \rho_s \rangle = \langle \rho_f \rangle + \langle \rho_m \rangle. \tag{6.2}$$

$$\tag{6.3}$$

Then the new properties are given by the following formulas

$$\langle e_m \rangle = \frac{\langle \rho_s \rangle \langle e_s \rangle - \langle \rho_f \rangle \langle e_f \rangle}{\langle \rho_m \rangle}, \tag{6.4}$$

$$\langle e_m^v \rangle = \frac{\langle \rho_s^v \rangle \langle e_s^v \rangle - \langle \rho_f^0 \rangle \langle e_f^0 \rangle}{\langle \rho_m^v \rangle}, \tag{6.5}$$

$$\langle e_m^c \rangle = \frac{\langle \rho_s^c \rangle \langle e_s^c \rangle - \langle \rho_f^0 \rangle \langle e_f^0 \rangle}{\langle \rho_m^c \rangle}. \tag{6.6}$$

where in the last two equation, $\langle \rho_s^v \rangle = 280$, $\langle \rho_s^c \rangle = 220$, $\langle \rho_m^v \rangle = 120$, $\langle \rho_m^c \rangle = 60$, $\langle \rho_f^0 \rangle = 160$, $\langle e_s^{v,c} \rangle$ are taken from TACOT, $\langle e_f^0 \rangle$ is from carbon fibers properties. This new set of properties is now used to simulate experiment of the Plasmatron on pyrolysing materials.

Plasmatron experiments on pyrolysing materials

Several test cases on carbon-phenolic samples were performed inside the Plasmatron. Different shapes (hemispherical, cylindrical), test gas (air, nitrogen) and test conditions (high and low pressure, high and low heat flux, subsonic and supersonic) has been investigated by Helber [13]. Once again a single test case was selected for the numerical simulation. The motivation for the choice of the case is the same as in Chap. 4 and also because the two test cases simulated in this work have closed operating conditions. The experimental test conditions of the carbon-phenol reference test case are given in Tab. 6.1.

Test name	gas	p_s	P_{el}	$\dot{q}_{cw}$	τ	T_w	$\dot{s}$	$\dot{m}$	ϵ
		hPa	kW	kW/m^2	s	K	μm/s	mg/s	
AS-A3a	air	200	163	1016	90.4	1845	36 ± 3	60.4	0.97

Table 6.1: Real Plasmatron test conditions for the reference test case (from Helber [13]). Asterm (AS) hemispherical sample, test gas, static pressure p_s, generator power P_{el}, mean cold wall heat flux $\dot{q}_{cw}$, sample exposure time τ, mean surface temperature T_w, recession rate $\dot{s}$, mass loss rate $\dot{m}$ and emissivity of the surface ϵ.

Simulation of Plasmatron experiments on carbon-phenolic material

Plasmatron carbon-phenol exepriments is reproduced in this section. A 2D configuration is considered in this case, as opposed to the previous Plasmatron simulations on carbon preform. For axisymmetric simulations, additional source terms must be considered, as explained in Sec. 2.3.1, that have not been implemented yet in the numerical solver for the case of a resin filled material.

The thermal decomposition laws used here are the ones presented in the previous chapter. Two fake resin species are used to track the different decomposition rate. The only gaseous species that is released from the decomposition is a single mixture of CO. No heterogeneous reactions with the gas and the fibers are considered here. For the short-time simulation presented in this section, this assumption remains valid considering that at the beginning of the ablation process, the fibers are protected by the resin and they do not react immediately. All the production of gas comes therefore only from pyrolysis reactions.

Computational domain

The computational domain and the boundary conditions are the same as in the previous simulations on carbon preform material, except that the mesh was refined at the interface considering the discussion from Sec. 4.3.1. The outlet boundary was also slightly shifted in order to keep away its influence on the flow field close to the end of the material. The numerical set-up and the performances of the simulation performed for the Plasmatron experiments on pyrolysing material are summarized in Tab. 6.2.

Nb of time steps	Nb of elemts	Nb of DOFs	Nb of CPUs	CPU time
81198	2250	$2250 \times 3 \times 12$ $(= 81000)$	12	≈ 2 weeks

Table 6.2: Summary of the computational performances and characteristics of Plasmatron experiment with pyrolysis.

The number of elements was increased due to the refinement at the boundary layer and the simulation time also increased drastically, emphasizing the need of improving the computational cost of such simulations in future works. This rise in the CPU time is also due to the higher number of degree of freedoms, coming from the two additional species of

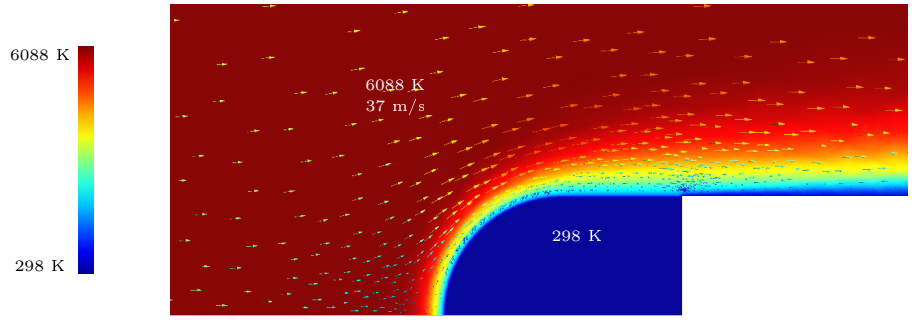

Figure 6.2: Thermal boundary layer around the thermal protection material (time = 0.4 s). Temperature ranges from 6088 K in the freestream to 298 K in the sample. Velocity magnitude is of the order of 37 m/s.

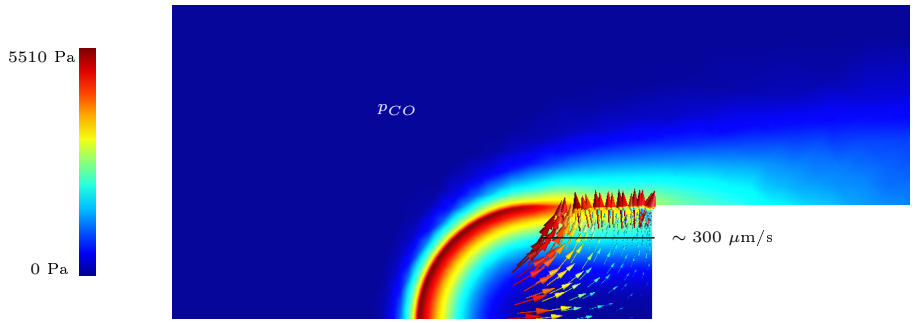

Figure 6.3: Production of pyrolysis gas due to thermal degradation of the composite ablator (time = 0.4 s). The flow field inside the porous medium is of the order of 300μm/s.

the resin that are used to track the thermal decomposition of the porous medium.

Results

First results of the Plasmatron experiment on pyrolysis experiments are presented in this section. The physical time reached after the simulation is equal to 0.4s and does not allow to compare the result with experiment. It was observed experimentally that the peak of the pyrolysis production was reached after 2.5 seconds after the injection of the sample and no steady-state of ablation is expected in this simulation.

Qualitative analysis

In Fig. 6.2, temperature field as well as the vector velocity field are represented. In Fig. 6.3, the pressure field of the pressure in CO, coming from the pyrolysis reactions, is given. The flow field inside the material sample can be observed once again. The increase of pressure is higher close to the stagnation line than at the shoulder of the sample, leading to an overall flow coming from the stagnation point towards the shoulders. Note the relatively low flow velocity, due to the fact that at 0.4s the blowing rate is still below its maximum.

Mole fractions along stagnation line

The mole fractions along the stagnation line for the different species in the fluid are extracted along the stagnation line and are shown in Fig. 6.4. The information about the

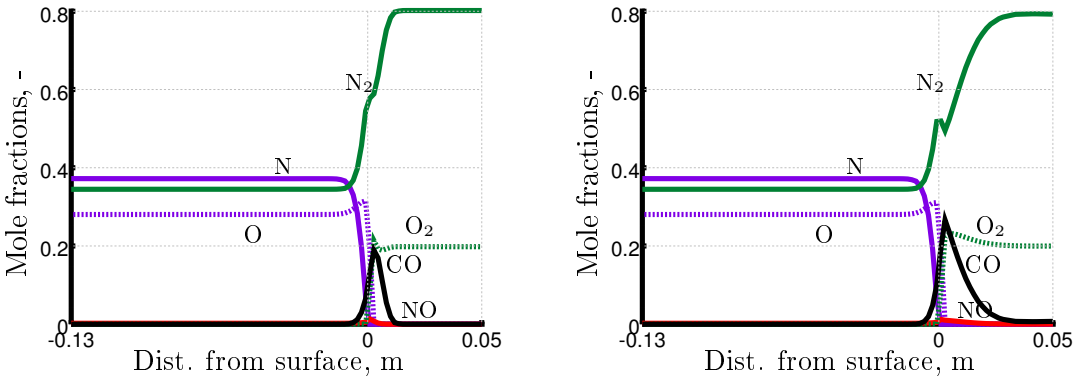

(a) $t = 0.01$ s (b) $t = 0.4$ s

Figure 6.4: Species mole fractions along the stagnation line at two different times of simulation.

chemical reaction are deduced from these two graphs. The sharp increase of CO due to the thermal degradation of the resin can be observed at the interface of the material. This peak increases with time as expected because the maximum of pyrolysis production is reached after 2.5s. The peak becomes wider also with time because species are at the same time diffused and convected inside the sample, inside which they were not present initially. Note that now, the O_2 species are not consumed inside the material anymore and this will lead to a sharp increase of pressure in the pyrolysis region inside the material sample, as it is shown below.

Total pressure along stagnation line

The total pressure along the stagnation line is shown in Fig. 6.5 at two different times of the simulation. Two main differences are observed compared to the previous case of the

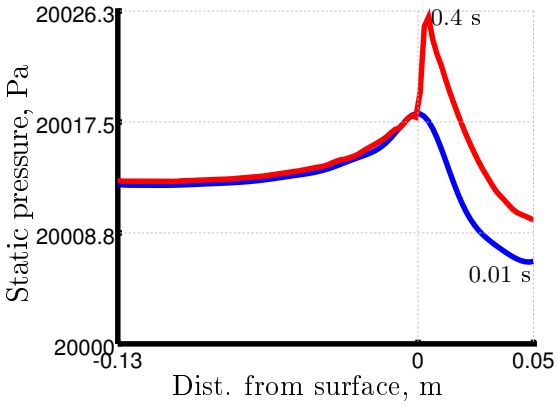

Figure 6.5: Pressure along the stagnation line at $t = 0$s and $t = 0.4$s.

simple preform experiment. The chemical species O and O_2 are not consumed anymore, as it was just observed, leading to a sharper increase of pressure. This maximum peak of pressure is expected to keep increasing with the blowing rate of pyrolysis.

Note that the peak of maximum pressure also shifts with time, because of the relatively fast recession of the virgin resin front inside of the material sample.

Review of the chapter

First simulation of pyrolysis experiments performed inside the Plasmatron has been successfully reproduced in this chapter. A new set of material properties valid for the unified approach with a mixture of air were derived. The need of the development of accurate data in future work was emphasized. The capability of the code to simulate the thermal degradation of the composite material was shown. Finally, quantities that can be extracted only using this unified approach were presented and a rapid increase of pressure due to pyrolysis blowing was observed.

Chapter 7

Conclusions and perspectives

In this last chapter, the main outcomes of this work are reviewed and some suggestions for future work are proposed.

Achievements

Simulation of Plasmatron carbon preform experiments

For the first time, a 2D axisymmetric simulation of Plasmatron experiments on an ablative carbon preform by means of a unified approach solver was presented. Such an approach has the novelty of solving both the flow and the solid phase in the same computational domain; this allows to capture the interactions between the two phases, that become important when investigating low-density thermal protection materials, with a better accuracy.

A Plasmatron experiment (1 Mw/m2 cold-wall heat flux and 200 mbar chamber static pressure) was numerically reproduced, showing that such a reproduction of the experimental set-up was possible using the unified approach implemented in Argo with DG methods. The Argo code correctly captured the increase in the temperature of the material surface but the agreement of the results with the experiments was shown to be sensitive to the definition of the surface position arising from the smoothing of the interface. Other quantities such as the creeping flow inside the pores, that would not be possible to quantify experimentally, were observed numerically showing the advantage of such unified approach.

However, it has to be noticed that low order polynomials were used for this development and debugging phase. In the future it will be certainly possible to repeat this analysis with higher order polynomials, exploiting the DG formulation of Argo.

Development and implementation of a pyrolysis model in a Discontinuous Galerkin solver

A model accounting for the thermal degradation (pyrolysis) and the char oxidation (ablation) of carbon based pyrolyzing materials was integrated into Argo. The model for the pyrolysis assumes different rate of decomposition; one solid mass conservation equation is added for each reaction. Once the material has completely pyrolyzed at a specific location, the charred material is assumed to be spread around the fibers and a model of cylindrical recession is used.

Two test cases were proposed to verify the implementation of the pyrolysis module. Both test cases were validated against the material response code Echion and showed good agreements with the results.

The first test case was performed on a non-pyrolyzing material and showed that material properties were correctly implemented. The code was able to reproduce a pure conduction problem of a material having different solid phase.

The second test case was performed on a pyrolyzing material and it was used to verify the implementation of the thermal degradation processes. No degradation of charred material was considered. Slight differences were observed in this case, explicable by the fact that a different, more accurate, momentum balance formulation is implemented in Argo.

It has to be stressed that the solver, using a unified approach accounting for the pyrolysis of a reacting porous medium, is the first of its kind to be developed and it opens the opportunity to a wide range of applications.

Perspectives for future work

Several questions were left open for future works and new perspectives were raised by the analysis of the numerical results. They are stated here as suggestion and improvement of this work.

- Concerning the reproduction of the Plasmatron experiment, the need for a better accuracy of the solution is required. It was shown that the mesh needed to be fine enough at the interface to catch the phenomena of recession, volume ablation and mass decrease. The length of ablation can be used to estimate the size of the smallest cell at the interface. Higher order polynomial can be used as well for improving the accuracy of the solution. An other important feature of the Argo code is the discontinuity of the interpolation [14]. Both mesh resolution and order of interpolation can be chosen locally, allowing to increase the accuracy of the solution only at the interface without increasing significantly the computation cost.

- Constant inlet conditions provided by the boundary layer edge solver were used. The influence of non-constant inlet profiles (e.g., provided by the ICP CoolFluiD solver) on the material ablation and heating is worthy to be investigated.

- In this work, the implementation using MPI showed the efficiency of the scalability of the Argo code. However, the simulation time was still too high to allow more complex sensitive analyses or uncertainty quantification. First improvements of the code would be to derive analytically the Jacobians associated to the source term, convective and diffusive fluxes in the case of the pyrolysis material that were not implemented during this work. Then, an analysis of the influence of the boundary conditions should be performed. In particular, we discussed the influence of the transient behaviour of the freestream flow and the generation of pressure waves that were severely limiting the time step at the beginning. It was also observed that the outlet BC was influencing the convergence.

- Verification test cases with multi-species component should be performed on the simple 1D geometry that was presented in Chap. 5. A thermal decomposition of the resin with pyrolysis gas mass fractions at equilibrium was implemented. During this work, it was observed that the test case was not converging when multi-species mixtures were used. A first clue in order to tackle this issue could be to investigate the value of the penalty parameter derived by Shahbazi [44]. Alternatively, an other method for the discretization of the diffusive terms, such as as the NSIP already implemented in Argo, should be tested as suggested in Sec. 3.2.3.

- The lack of further verification test cases in literature for flow-material solver did not allow the comparison of the full test case of a pyrolyzing material. In particular, more accurate thermodynamic and transport properties are missing for flow-material solvers. Properties for the theoretical material TACOT were used and the results showed the good agreement with state-of-the art material response codes. However the TACOT properties are already an average of fluid and solid properties. For the unified approach implemented in Argo, properties valid only for the solid material are required. Experimental investigated of material properties are therefore required. This could provide a database that will allow the different numerical codes to be compared.

- Treatment of material a fluid in the same domain of computation accounting for pyrolysis of the material raises several questions about the treatment of the degradation reactions at the interface. Indeed, the Goldstein laws used in this work are proportional to the inverse of the virgin density (Eq. 2.33), which tends to zero in the freestream. This leads to numerical instabilities far away from the surface that have to be avoided. The smoothing itself of the surface of the porous material raises also the problem of the production rate at the the surface. Smoothing the production rate at the interface, in order to avoid numerical instabilities due to a division by zero, leads to a production rate that is lower in the smoothing region. Therefore, heterogeneous reactions below the surface may be triggered earlier because of a fastest rate of decomposition.

- The unified approach allows to have ablation that occur in volume and not only at the surface as previous material response codes. Therefore, determining when heterogeneous reactions start after the pyrolyzing process is required and this raises several issues. It seems that using a threshold value is not very accurate and the time where oxidation reactions starts will be very sensitive to that value. It could be possible that a mixed region where both pyrolysis and heterogeneous reactions occur is taking place, but no data were found in literature.

- The implementation of a module accounting for pyrolysis open the possibility of many application of the Argo solver. First applications could be in the field of material combustion. Experiments of Trick and Saliba could be first tried to be reproduced [47], [48]. Sensitivity analyses on such experiment could help to determine material properties. In particular, the Argo solver might be a very useful tool for uncertainty quantification studies:

  - Propagation of uncertainties on boundary conditions (inlet temperature) and on model parameters with ANOVA approach.
  - Development of surrogate models based on CFD simulations (Polynomial chaos, Krigging).
  - Inverse problem: inference of some models parameters from experiment in a stochastic framework.

Appendix A

Parallelisation of Argo

To overcome node limit and scale to cluster achitectures, the parallelization of the code using Message Passing Interface (MPI) library was successfully implemented by Corentin [5]. A hybrid parallelisation using OpenMP directives could also be investigated but the Mutation++ library is not yet available with OpenMP. This short study proves the scalability of the DGAblation module. It is shown that a speedup is observes for a low number of elements by processors. However the solution is not converging when scaling to a high number of threads. The result of the parallelisation study are presented below.

Comparison of speedup

DGM has a great parallel scalability due to its data locality and the speratation between the volume terms (that does not require any communication) and the interface terms that allows to optimise the parallelization method easily. The sequential optimization was eprformed by Hillewaert [14] and the parallel efficiency of the solver was studied and implemented by Carton de Wiart [5].

The partitioning strategy for a MPI parallelization is to divide the computational domain in a set of subdomains that are independantly accessed by only one process. The partitioning of the domain is performed using the finite element mesh generator Gmsh [11].

The speedup is computed by the ratio of the computational time T_s (wall clock) of serial (one single processor) and the computational time in parallel T_p for a given number of processors n

$$S(n) = \frac{T_s}{T_p(n)}, \tag{A.1}$$

where $T_s = T_p(1)$. The number of time steps after which the speedup is compared is equal to 10. The study is performed on the Plasmatron test case (see Tab. 4.2) with $\Delta_t = 10e\text{-}4$ starting from a quasi-steady state solution (i.e. the freestream conditions are almost steady) using first order elements. A ILU preconditioning is used on the NR and the GMRES algorithms. Note that the use of other preconditioners could be investigated as well as the effect of their parallization on the convergence of the solution. This is however not performed in this work.

Fig. A.1 compares the CPU time per time step and the speedup for an increasing number of cores used. A speedup is observed for a number of processors up to 40 on the number of time steps observed. Note that for 40 processors, the number of elements

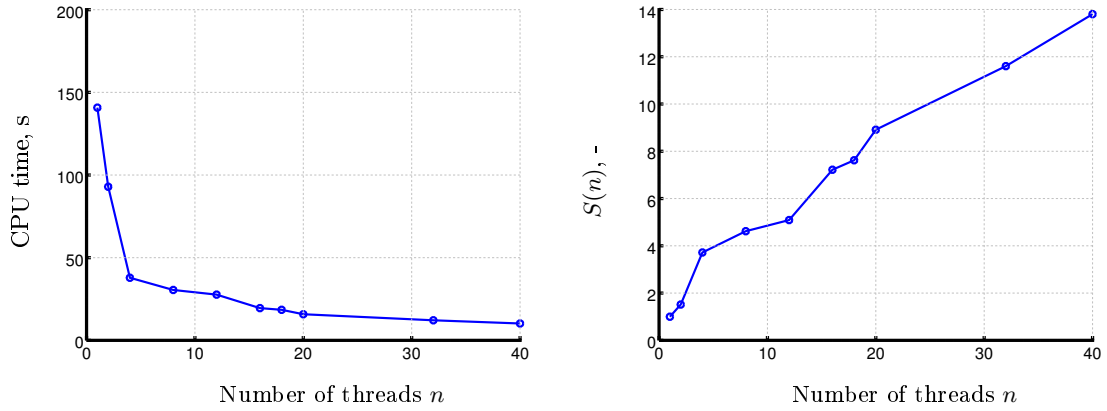

Figure A.1: CPU time and Speedup for a increasing number of threads on the VKI cluster ClusterVision.

per thread is ~ 38, which is much lower than the several hundreds of elements per threads assumed to be the optimum value for the speedup [5]. This high scalability is explained by the fact that this study was performed on a large number of DOFs due to the number of species considered in the mixture. It is expected that increasing the DOFs by increasing the number of mass equations in the VANS system will increase the scalability of the DGM.

However, for a number of processors higher than 16 it was observed that the solver was not converging at some iterations of the NR solver. This non-convergence is attributed to the splitting of preconditioner of the system between the processors that may affect the convergence of the solver, especially for a high number of threads. It would be therefore useful to study the influence of the preconditioning matrix on the convergence of the algorithm when the problem is scaled on a high number of processors.

Some attention should also be paid in the future to the scalability of the problem for higher order elements as well as using finer meshes, that both increase the number of DOFs in the system.

Bibliography

[1] John D. Anderson. *Hypersonic and High Temperature Gas Dynamics.* AIAA Education Series, second edition, 2006.

[2] P. F. Barbante and O. Chazot. Flight Extrapolation of Plasma Wind Tunnel Stagnation Region Flowfield. *Journal of Thermophysics and Heat Transfer*, 20(3):493–499, 2006.

[3] B. Bottin, M. Carbonaro, S. Paris, V. Vanderhaegen, A. Novelli, and D. Vennemann. Vki 1.2 MW Plasmatron Facility for the Thermal Testing of TPS Materials. *3^{rd} European Workshop on Thermal Protection Systems*, March 1998.

[4] B. Bottin, O. Chazot, M. Carbonaro, V. Van Der Haegen, and S. Paris. The VKI Plasmatron Characteristics and Performance. Technical report, von Karman Inst. for Fluid Dynamics, Rhode-Saint-Genèse (Belgium), 2000.

[5] C. Carton de Wiart. *Towards a discontinuous Galerkin solver for scale-resolving simulations of moderate Reynolds number flows, and application to industrial cases.* Phd thesis, Université catholique de Louvain, 2014.

[6] Y.-K. Chen and F. S. Milos. Ablation and thermal response program for spacecraft heatshield analysis. *Journal of Spacecraft and Rockets*, 36(3):475–483, 1999.

[7] J. Coheur. Sensitivity Analysis and Uncertainty Quantification of Plasma Jet Instabilities in the VKI Plasmatron. Master's thesis, Université de Liège and Von Karman Inst. for Fluid Dynamics, 2015.

[8] M. A. Covington, J. M. Heinemann, H. E. Goldstein, Y.-K. Chen, I. Terrazas-Salinas, J. A. Balboni, J. Olejniczak, and E. R. Martinez. Performance of a Low Density Ablative Heat Shield Material. *Journal of Spacecraft and Rockets*, 45(2):237–247, 2008.

[9] A. Dal Bianco, D. D'Ambrosio, and V. Mareschi. A fully implicit material response code with ablation and prolysis for simulation of thermal protection systemss. In *8th European Symposium on Aerothermodynamics for Space Vehicles*, Lisboa (Portugal), 2-6 March 2015.

[10] G. Duffa. *Ablative Thermal Protection Systems Modeling.* AIAA Education Series, 2013.

[11] C. Geuzaine and J.-F. Remacle. Gmsh: a three-dimensional finite element mesh generator with built-in pre- and post- processing facilities. *International Journal for Numerical Methods in Engineering*, 79(11):1309–1331, 2009.

[12] H. E. Goldstein. Pyrolysis Kinetics of Nylon 6-6, Phenolic Resin, and Their Composites. *Journal of Macromolecular Science: Part A - Chemistry*, 3(4):649–673, 1969.

[13] B. Helber. *Material Response Characterization of Low-Density Ablators in Atmospheric Entry Plasmas.* Phd thesis, Vrije Universiteit Brussel & von Karman Institute for Fluid Dynamics, Belgium, 2016.

[14] K. Hillewaert. *Develoment of the discontinuous Galerkin method for large scale/high-resolution CFD and acoustics in industrial geometries.* Phd thesis, UniversitÃĺ catholique de Louvain, 2013.

[15] F. Homann. The effect of high viscosity on the flow around a cylinder and around a sphere. Technical memorandum 1334, NACA, 1952. Translation of "Der Einfluss grosser Zähigkeit bei der Strömung um den Zylinder und um die Kugel", ZAMM, vol. 16, no. 3, June 1936.

[16] J. T. Howe. Hypervelocity Atmospheric Flight: Real Gas Flow Fields. Technical memorandum 101055, NASA Ames Research Center, Moffett Field, CA, USA, 1989.

[17] R. M. Kendall, E. P. Barlett, R. A. Rindal, and C. B. Moyer. An Analysis of the Coupled Chemically Reacting Boundary Layer and Charring Ablator: Part I. CR-1060, NASA, 1968.

[18] A. F. Kolesnikov. Conditions of Simulation of Stagnation Point Heat Transfer from a High-Enthalpy Flow. *Fluid Dyn., No. 28 (1), 131-137*, 1993.

[19] J. Lachaud, I. Cozmuta, and N. N. Mansour. Multiscale approach to ablation modeling of phenolic impregnated carbon ablators. *Journal of Spacecraft and Rockets*, 47(6):910–921, 2010.

[20] J. Lachaud, T. E. Magin, I. Cozmuta, and N. N. Mansour. A Short Review of Ablative-Material Response Models and Simulation Tools. In L. Ouwehand, editor, *7th European Symposium on Aerothermodynamics*, SP-692, Brugge, Belgium, May 2011. ESTEC-ESA.

[21] J. Lachaud, A. Martin, I. Cozmuta, and B. Laub. Ablation Workshop Test Case. In *4th Ablation Workshop*, Albuquerque, New Mexico, 1-3 March 2011.

[22] J. Lachaud, A. Martin, T. Van Eekelen, and I. Cozmuta. Ablation test-case series #2. In *5th Ablation Workshop*, Lexington, Kentucky, 28 March 2012.

[23] J. Lachaud, T. van Eekelen, J. B. Scoggins, T. E. Magin, and N. N. Mansour. Detailed chemical equilibrium model for porous ablative materials. *International Journal of Heat and Mass Transfer*, 90:1034–1045, 2015.

[24] A. Lani. *An object oriented and high performance platform for aerothermodynamics simulation.* Phd thesis, Université Libre de Bruxelles & Von Karman Institute for Fluid Dynamics, Belgium, 2008.

[25] J. Lauchaud and N. N. Mansour. Porous-material aalysis toolbox based on OpenFOAM and applications. *Journal of Thermophysics and Heat Transfer*, 28(2):191–202, 2014. Ahead of print.

[26] Weijie Li, Haiming Huang, Ye Tian, and Zhe Zhao. Nonlinear analysis on thermal behavior of charring materials. *International Journal of Heat and Mass Transfer*, 84:245–252, 2015.

[27] W.-S. Lin. Quasi-steady solutions for the ablation of charring materials. *International Journal of Heat and Mass Transfer*, 50:1196–1201, 2007.

[28] T. Magin. *A Model for Inductive Plasma Wind Tunnels*. Phd thesis, Université Libre de Bruxelles & Von Karman Institute for Fluid Dynamics, Belgium, 2004.

[29] T. E. Magin. Physical Gas Dynamics. Lecture notes. Von Karman Institute for Fluid Dynamics, 2010-2011.

[30] T. E. Magin. Cooled Pitot probe in air plasma jet. In *I³MS Seminar Series*, Aachen, Germany, 13 July 2015.

[31] T. E. Magin, L. Caillault, A. Bourdon, and C. O. Laux. Nonequilibrium Radiative Heat Flux Modeling for the Huygens Entry Proble. *J. Geophys. Res.*, 111(E07S12), 2006.

[32] A. Martin. Volume averaged modeling of the oxidation of porous carbon fiber material. *Mechanical Engineering Faculty Publications*, Paper 13, 2013.

[33] Mersen. Calcarb rigid carbon thermal insulation. Technical guide HT 29 GB 0121, Mersen, 2011.

[34] F. S. Milos and Y.-K. Chen. Ablation, thermal response, and chemistry program for analysis of thermal protection systems. *Journal of Spacecraft and Rockets*, 50(1):137–149, 2013.

[35] A. D. Omidy, F. Panerai, J. Lachaud, N. N. Mansour, and A. Martin. Effects of water phase change on the material response of low-density carbon-phenolic ablators. *Journal of Thermophysics and Heat Transfer*, pages 1–6, 2016. Ahead of print.

[36] R. Palaninathan and S. Bindu. Modeling of mechanical ablation in thermal protection systems. *Journal of Spacecraft and Rockets*, 42(6):971–979, 2005.

[37] F. Panerai. *Aerothermochemistry Characterization of Thermal Protection Systems*. Phd thesis, Università Degli Studi Di Perugia, 2012.

[38] F. Panerai, A. Martin, N. N. Mansour, S. A. Sepka, and J. Lachaud. Flow-tube oxidation experiments of the carbon preform of a phenolic-impregnated carbon ablator. *Journal of Thermophysics and Heat Transfer*, 28(2):181–190, 2014.

[39] C. Park, R. L. Jaffe, and H. Partridge. Chemical-kinetic parameters of hyperbolic earth entry. *Journal of Thermophysics and Heat Transfer*, 15(1):76–90, 2001.

[40] H. Ritter, O. Bayle, Y. Mignot, E. Boulier, P. Portela, J.-M. Builly, and R. Sharda. Ongoing European developments on entry heatshields and TPS materials. In *8th International Planetary Probe Workshop*, Portsmouth, Virginia, USA, 6-10 June 2011.

[41] B. Rivière. *Discontinuous Galerkin methods for solving elliptic and parabolic equations - theory and implementation*. Society for Industrial and Applied Mathematics. 2008.

[42] P. Schrooyen. *Numerical Simulation of Aerothermal Flows Through Ablative Thermal Protection Systems*. Phd thesis, Université Catholique de Louvain & von Karman Institute for Fluid Dynamics, Belgium, 2015.

[43] J. Scoggins and T. E. Magin. Development of Mutation++: Multicomponent thermodynamic and transport property library for ionized plasmas written in C++. In *11th AIAA/ASME Joint Thermophysics and Heat Transfer Conference*, Atlanta, GA, 16-20 June 2014. AIAA Paper 2014-1966.

[44] K. Shahbazi. An explicit expression for the penalty parameter of the interior penalty method. *Journal of Computational Physics*, 205:401–407, 2004.

[45] M. Stackpoole, S. Sepka, I. Cozmuta, and D. Kontinos. Post-Flight Evaluation of Stardus Sample Return Capsule Forebody Heatshield Material. *Journal of Thermophysics and Heat Transfer*, 24(4):694–707, 2010.

[46] H. K. Tran, C. E. Johnson, D. J. Rasky, F. C. L. Hui, M.-T. Hsu, T. Chen, Y. K. Chen, D. Paragas, and L. Kobayashi. Phenolic Impregnated Carbon Ablators (PICA) as Thermal Protection Systems for Discovery Missions. Technical Memorandum TM 110440, NASA Ames Research Center, 1997.

[47] K. A. Trick and T. E. Saliba. Mechanisms of the pyrolysis of phenolic resin in a carbon/phenolic composite. *Carbon*, 33(11):1509–1515, 1995.

[48] K. A. Trick, T. E. Saliba, and S. S. Sandhu. A kinetic model of the pyrolysis of phenolic resin in a carbon/phenolic composite. *Carbon*, 35(3):393–401, 1997.

[49] A. Turchi, B. Helber, Munafò, and Magin T. E. Development and Testing of an Ablation Model Based on Plasma Wind Tunnel Experiments. In *11th AIAA/ASME Joint Thermophysics and Heat Transfer Conference*, Atlanta, GA, 16-20 June 2014. AIAA Paper 2014-2125.

[50] A. Turchi, J. J. Matesanz Saiz, T. E. Magin, and O. Chazot. On the flight extrapolation of stagntion-point ablative material plasma wind tunnel tests. In *8th European Symposium on Aerothermodynamics for Space Vehicles*, Lisbon, Portugal, 2-6 March 2015.

[51] Stephen Whitaker. *The Method of Volume Averaging*, volume 13 of *Theory and Applications of Transport in Porous Media*. Springer Netherlands, 1st edition, 1999.

[52] C. Zuber, T. Rothermel, and L. Walpot. A light-weight ablative material for research purposes. In *6th Ablation Workshop*, Urbana-Champaign, IL., 10 - 11 April 2014.